Phasor-Based Adaptive Control of a Test-Feeder Distribution Network

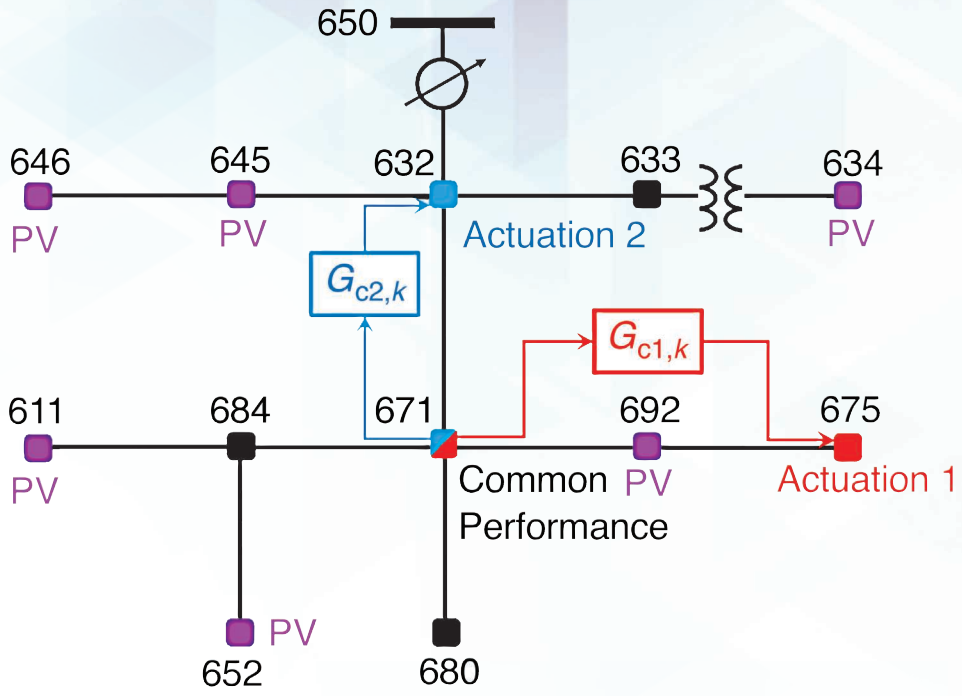

APPLICATION OF RETROSPECTIVE COST ADAPTIVE CONTROL TO THE IEEE 13-NODE TEST FEEDER

SYED ASEEM UL ISLAM, ELIZABETH L. RATNAM, ANKIT GOEL, and DENNIS S. BERNSTEIN

Control in the power distribution system is needed to match the generation of electricity (that is, supply) with the demand for power (that is, load) at all times while maintaining a high level of power quality [1] (see "Summary"). The complexity of controlling the electric distribution system increases when distributed intermittent energy sources, such as solar photovoltaics (PVs), displace large-scale dispatchable generation [2]–[10]. If the supply from distributed resources exceeds the time-varying demand across a feeder, then the feeder-level voltage will increase. In extreme cases, large voltage increases will trigger the disconnection of distributed generation to protect electrical equipment and ensure customer safety. Consequently, coordinating renewable energy sources that are distributed throughout the distribution system—to match real-time demand across an entire power network—brings the additional challenge of maintaining a high level of supply reliability.

Digital Object Identifier 10.1109/MCS.2019.2913611
Date of publication: 18 July 2019

To accommodate both traditional and alternative energy sources in the electrical distribution system, it is necessary to improve the power quality across a distribution feeder. More specifically, both time-varying generation and demand can be viewed as disturbances [11]–[13] since they cause undesirable fluctuations and offsets in the voltage magnitudes and angles in a three-phase power network. To improve power quality and thus prevent damage to electrical equipment on the customer and supply sides, voltage magnitudes must be corrected. Furthermore, to ensure that thermal constraints are not exceeded and reverse power flows are controlled, voltage angles must be corrected. The goal of this article is to develop a methodology for correcting voltage magnitudes and angles in three-phase power, thus improving power quality.

Model-based methods for the optimization and control of power systems are given in [14] and [15]. In contrast to these methods, this article develops a methodology that reflects conditions that often occur when a controller is developed for a physical system. In particular, a representative simulation of the system that captures key details may be available; however, this simulation may be erroneous due to unmodeled dynamics and unknown parameters. In addition, the representative simulation of the system may be available only in the form of a simulation code, the details of which are not accessible to the user. This can occur when the code uses extensive lookup tables, involves complex physics, or is proprietary. In these cases, the simulation is effectively an opaque executable simulation.

Motivated by these constraints, an approach whereby an adaptive controller is tuned based on the nominal simulation is considered in this article. However, this approach does not attempt to identify the system, which may be a nontrivial task due to its complexity. The simulation can be run multiple times to tune the weightings of the adaptive controller, which is referred to as *nominal simulation tuning* (NST). The weightings of the adaptive controller obtained under NST are then fixed, and the robustness and performance of the adaptive controller with the fixed weightings are evaluated through subsequent simulations based on modifications of the nominal simulation, which is referred to as *perturbed simulation testing* (*PST*). These modifications are chosen to reflect off-nominal conditions of the model, commands, disturbances, and noise that can potentially occur in real-world operation. These off-nominal conditions are merely representative, however, and not intended to be exhaustive. Therefore, PST provides confidence in the ability of retrospective cost adaptive control (RCAC) to adapt to the actual real-world system. Without knowledge of a model set that contains the actual real-world system, however, this approach does not guarantee success.

If the performance and robustness of the fixed-weighting adaptive controller are found to be acceptable for the perturbed simulations, then the adaptive controller is considered viable for the real-world system. The success of this approach depends on the extent to which the nominal and off-nominal simulations capture the key features of the real-world system. Furthermore, success in real-world operation depends on the ability of the adaptive controller to accommodate features of the real-world system that were not captured by either the nominal or perturbed simulations. The difference between this methodology and classical control synthesis is the limited access that the engineer has to plant modeling details, relying, to a large extent, on the ability of the adaptive controller to adapt to discrepancies among the nominal simulations, the perturbed simulations, and the real-world system.

This article applies RCAC to the IEEE 13-node test feeder (IEEE13NTF), one of several internationally recognized and widely studied distribution system models [16]. Estimation, optimization, fault analysis, and control studies using IEEE13NTF are given in [17]–[30]. This three-phase, four-wire IEEE13NTF model captures the unbalanced nature of the distribution network with single-phase laterals and single-phase loads. Numerical testing of this model shows that convergence after a load disturbance is typically achieved in fewer than approximately 10 steps. Because of the nonlinearity and complexity of the three-phase power flows in this model, this article views IEEE13NTF as an opaque executable simulation, with no access to the underlying code and equations. The version of IEEE13NTF used in this article is provided by the OPAL-RT RT-Lab ePHASORSIM package [31]. This version of IEEE13NTF is proprietary, and the underlying code is inaccessible.

Summary

An electrical grid consists of multiple interconnected components that provide and use energy. A key concern for these systems is the ability to maintain the desired voltage magnitudes and angles throughout the grid in the presence of time-dependent disturbances in the form of renewable energy sources. This is a decentralized feedback control problem, where modeling information is limited by the changing topology and parameters of the grid. We consider command-following and disturbance-rejection problems for a standard grid model, the IEEE 13-node test-feeder model. The model is quasi-static due to the assumption of fast transient response. Retrospective cost adaptive control (RCAC) is applied in both centralized and decentralized control architectures, where each multiple input, multiple output controller has six inputs and six outputs, due to the need to regulate the magnitude and angle of three-phase power at each power node. The performance of RCAC is evaluated under conditions of extremely limited model information.

The control objective for IEEE13NTF is to achieve setpoint command-following for three-phase voltage magnitude and angle in the presence of load and generation disturbances. To meet the control objective, we consider both single-controller and decentralized dual-controller architectures with various choices of the performance, actuation, and disturbance nodes. The performance and actuation nodes are three phase, and the disturbance nodes are either single or three phase. The performance variables at each performance node are the command-following errors for the three voltage magnitudes and three voltage angles.

The approach of this article is based on RCAC, which is a data-driven, adaptive control method for output-feedback stabilization, command-following, and disturbance rejection [32], [33]. For single-input, single-output (SISO) linear plants, RCAC uses minimal modeling information, namely, the sign of the leading numerator coefficient, relative degree, and nonminimum-phase (NMP) zeros.

The objective of this article is to apply NST and PST based on RCAC to the IEEE13NTF model. As explained in [32], the first step in applying RCAC to the IEEE13NTF model is to construct the target model G_f for the intercalated transfer function. Within the context of linear systems, this modeling information contains knowledge about the leading signs, relative degree, and NMP zeros. As shown in [32], [34], and [35], RCAC is also effective on nonlinear systems with input and feedback nonlinearities. For the IEEE13NTF model, the required modeling information is obtained from a single simulation scenario. The relevant information consists of the sign of the first impulse-response matrix of the three-phase voltage magnitudes and angles, in response to an impulse in the active and reactive power. Specifically, a single 6×6 impulse-response matrix H_1 is used to construct a finite-impulse-response (FIR) target model G_f. The dependence of the closed-loop performance on H_1 is examined by determining those components of H_1 that can be removed without adverse effect on the performance of the nominal simulation. This investigation leads to a sparse approximation, $\hat{H}_1$, of H_1. In fact, $\hat{H}_1$ is diagonal for a specific pairing between the load actuation input and the voltage magnitude and angle. This procedure, along with selection of the controller order and structure and additional weightings, yields the fixed controller tuning for use in PST.

Next, the nominal simulation is perturbed in various ways that reflect variations in how RCAC may be used in the real-world system. Specifically, the controller structure and weightings obtained from NST are first applied in a centralized architecture, where a single multiple-input, multiple-output (MIMO) controller is applied between selected actuation and performance nodes. Next, a pair of MIMO subcontrollers is applied in a decentralized architecture, where each RCAC subcontroller operates independently of the other subcontroller, without information exchange or hierarchical coordination. In particular, we apply two RCAC subcontrollers in a decentralized architecture to determine the possibility of adverse interactions between controllers due to the lack of communication. In both scenarios, the only modeling information used by RCAC is the sparse matrix $\hat{H}_1$ used to define G_f.

In both the centralized and decentralized scenarios, the control input at each actuation node is the active and reactive power extracted from each of the three phases. The feedback controller that connects each performance node to a corresponding actuation node is, therefore, a six-input, six-output MIMO controller. Each 6×6 controller is fully populated and thus consists of 36 SISO controllers, each of which is a linear, strictly proper, discrete-time dynamic compensator. Since RCAC adapts the coefficients of the controller, it is a linear time-varying controller; however, after the controller coefficients converge, it is a linear time-invariant controller. For decentralized control, each subcontroller is of the same type. As a test of the decentralized, fixed-structure subcontroller, we consider the case of multivariable actuator saturation, which corresponds to a physical limitation on the maximum power flow through a four-quadrant operation inverter. The level and form of the saturation are unknown to the subcontrollers.

Finally, we consider decentralized control in the case in

TABLE 1 **A summary of simulations used for nominal simulation tuning (NST) and perturbed simulation testing (PST). The first simulation represents the case chosen for NST. Each subsequent simulation represents a perturbation of the nominal simulation in terms of the disturbance signals; actuator saturation levels; and choice of disturbance, actuation, and performance nodes.**

Simulation	Centralized (C) or Decentralized (D)	Disturbance Nodes	Actuation Nodes	Performance Nodes	Sensor Noise	Saturation
NST	C	611, 634	675	671	Yes	No
PST 1	C	611, 634	632	633	Yes	No
PST 2	D	611, 634	632, 675	633, 671	Yes	No
PST 3	D	611, 634	632, 675	671	Yes	Yes
PST 4	D	Photovoltaics at 611, 634, 645, 646, 652, 692	632, 675	671	Yes	No

which the IEEE13NTF model includes significant PV penetration. PV generation data from Pecan Street [36], an online repository of data collected from real consumers and producers of electricity, are used. The data from various consumers/producers are aggregated to simulate loads on nodes in the IEEE13NTF model. This method is used to simulate 70.61% PV penetration in the distribution system. A summary of the numerical simulations is presented in Table 1. The nominal simulation is run multiple times to tune the RCAC weightings, select the controller structure, and construct the sparse G_f. PSTs 1–4 are run once by using the controller from NST with the modifications to the nominal simulation presented in Table 1.

The contribution of this article is the application of RCAC to IEEE13NTF, for which the only modeling information used is a sparse approximation of the first impulse-response coefficient. An additional contribution of this article is the use of a controller structure that simplifies the controller structure used in [32]. Specifically, the approach of [32] specifies the order of the controller in MIMO input–output model form; otherwise, the controller is unstructured in terms of the allowable locations of its poles and zeros. In contrast, this article employs a variation of [32], called *fixed-structure RCAC*, whereby the user can specify the internal structure of each SISO entry of the 6×6 MIMO controller. Since each SISO entry of the 6×6 MIMO controller is specified as either a proportional-integral (PI) controller or a second-order infinite-impulse-response (IIR) controller, this extension reduces the complexity of feedback control of IEEE13NTF.

IEEE13NTF MODEL

Consider the nonlinear, time-varying, discrete-time plant

$$x(k+1) = f(x(k), u(k), d(k), k), \tag{1}$$

$$y_0(k) = g(x(k), u(k), d(k), k), \tag{2}$$

$$y_{\mathrm{n}}(k) = y_0(k) + v(k), \tag{3}$$

$$z(k) \triangleq r(k) - y_{\mathrm{n}}(k), \tag{4}$$

where $k \geq 0$ is the step, $x(k) \in \mathbb{R}^n$ is the state, $u(k) \in \mathbb{R}^{l_u}$ is the control input, $f : \mathbb{R}^n \to \mathbb{R}^n$ and $g : \mathbb{R}^n \to \mathbb{R}^n$ are nonlinear functions that represent the IEEE13NTF model, $d(k) \in \mathbb{R}^{l_d}$ is the disturbance, $y_0(k) \in \mathbb{R}^{l_y}$ is the plant output, $y_{\mathrm{n}}(k) \in \mathbb{R}^{l_y}$ is the measurement, $r(k) \in \mathbb{R}^{l_y}$ is the command, $v(k) \in \mathbb{R}^{l_y}$ is the sensor noise, and $z(k) \in \mathbb{R}^{l_y}$ is the measured error, which is also the performance variable. Note that l_u, l_d, and l_y are the dimensions that represent the control, disturbance, and measurement vectors, respectively. The model in (1)–(4) can be viewed as a synchronously sampled, sampled-data version of IEEE13NTF shown in Figure 1, where the sensing, actuation, and load/generation disturbances are on physically separated nodes. IEEE13NTF is a quasi-static model that requires the iterative solution of a set of nonlinear algebraic equations. Therefore, the algebraic

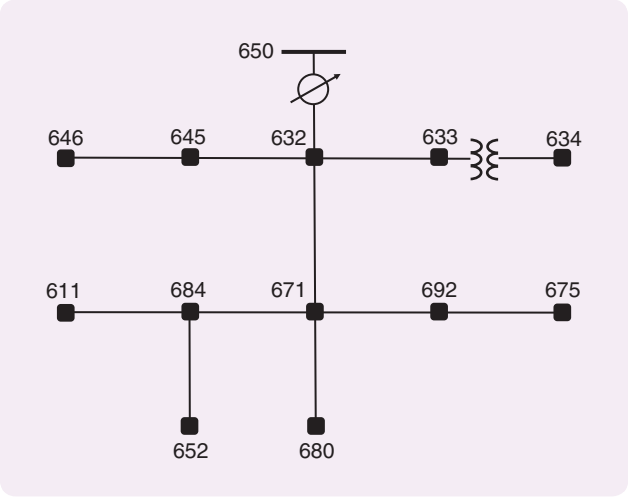

FIGURE 1 The IEEE 13-node test-feeder model. The model used for this article is provided by the OPAL-RT RT-Lab ePHASORSIM package.

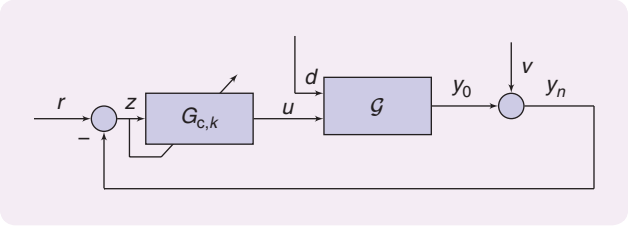

FIGURE 2 A block diagram representation of the adaptive servo problem with the adaptive controller $G_{c,k}$ and IEEE 13-node test feeder $\mathcal{G}$.

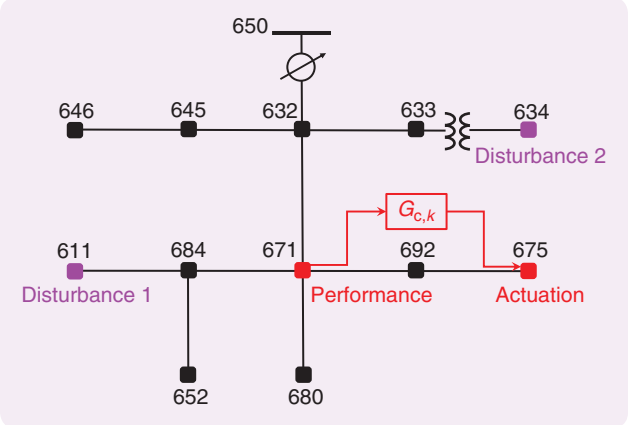

FIGURE 3 Nominal simulation tuning: at node 675, the controller $G_{c,k}$ can add or remove active and reactive power. At node 671, the controller $G_{c,k}$ has access to the voltage magnitude and angle measurements, where the voltage angles are relative to the slack bus at node 650. At nodes 611 and 634, the active and reactive power is varied, which represents an unmodeled load disturbance.

Fixed-Structure Retrospective Cost Adaptive Control Algorithm

CONTROLLER STRUCTURE

Define the dynamic compensator

$$u(k) = \Phi(k)\theta(k), \tag{S1}$$

where $\Phi(k) \in \mathbb{R}^{l_u \times l_\theta}$ is the regressor matrix constructed from past $y(k)$ and possibly past $u(k)$ data, and $\theta(k) \in \mathbb{R}^{l_\theta}$ is the controller coefficient vector.

RETROSPECTIVE PERFORMANCE

Define the retrospective control

$$\hat{u} \triangleq \Phi(k)\hat{\theta}, \tag{S2}$$

where $\hat{\theta} \in \mathbb{R}^{l_\theta}$ is determined by minimizing the retrospective cost function (S8). Using the retrospective control, define the retrospective performance variable as

$$\hat{z}(k,\hat{\theta}) \triangleq z(k) - G_{\mathrm{f}}(\mathbf{q})[u(k) - \hat{u}(k)], \tag{S3}$$

where $z(k), \hat{z}(k) \in \mathbb{R}^{l_z}$ and $u(k), \hat{u}(k) \in \mathbb{R}^{l_u}$. The optimal controller coefficient vector $\hat{\theta}_{\mathrm{opt}}(k)$, which is obtained by retrospective optimization (explained in the following section), yields the updated controller with coefficients $\theta(k+1) = \hat{\theta}_{\mathrm{opt}}(k)$ to be used at the next time step.

The $n_z \times n_u$ finite-impulse-response filter G_{f} of order n_{f} has the form

$$G_{\mathrm{f}}(\mathbf{q}) \triangleq \sum_{i=1}^{n_{\mathrm{f}}} N_i \mathbf{q}^{-i}, \tag{S4}$$

where N_i is an $l_z \times l_u$ matrix and $\mathbf{q}$ is the forward-shift operator. Equation (S3) can be rewritten as

$$\hat{z}(k,\hat{\theta}) \triangleq z(k) - N[\bar{U}(k) - \bar{\Phi}(k)\hat{\theta}], \tag{S5}$$

where

$$N \triangleq [N_1 \ \cdots \ N_{n_{\mathrm{f}}}] \tag{S6}$$

$$\bar{\Phi}(k) \triangleq \begin{bmatrix} \Phi(k-1) \\ \vdots \\ \Phi(k-n_{\mathrm{f}}) \end{bmatrix}, \quad \bar{U}(k) \triangleq \begin{bmatrix} u(k-1) \\ \vdots \\ u(k-n_{\mathrm{f}}) \end{bmatrix}, \tag{S7}$$

where $N \in \mathbb{R}^{l_z \times n_{\mathrm{f}} l_u}$, $\bar{\Phi}(k) \in \mathbb{R}^{n_{\mathrm{f}} l_u \times l_\theta}$, and $\bar{U}(k) \in \mathbb{R}^{n_{\mathrm{f}} l_u}$.

RETROSPECTIVE COST

Using the retrospective performance variable $\hat{z}(k,\hat{\theta})$ defined by (S3), define the cumulative retrospective cost function as

$$J(k,\hat{\theta}) \triangleq \sum_{i=1}^{k} \hat{z}^{\mathrm{T}}(i,\hat{\theta}) R_z \hat{z}(i,\hat{\theta}) + \sum_{i=1}^{k} (\Phi(i)\hat{\theta})^{\mathrm{T}} \bar{R}_u \Phi(i)\hat{\theta} + \hat{\theta}^{\mathrm{T}} \bar{R}_\theta \hat{\theta}, \tag{S8}$$

where $\bar{R}_\theta$ is positive definite, R_z is positive definite, and $\bar{R}_u$ is positive semidefinite. Recursive minimization of (S8) is used to update the controller coefficient vector $\hat{\theta}$. The following result uses recursive least squares to obtain the minimizer of (S8).

Proposition

Let $P(0) = \bar{R}_\theta^{-1}$. Then, for all $k \geq 1$, the retrospective cost function (S8) has the unique global minimizer $\hat{\theta}_{\mathrm{opt}}(k)$, which is given by

$$P(k) = P(k-1)[I_{l_\theta} - \gamma^{\mathrm{T}}(k)\beta(k)\gamma(k)P(k-1)], \tag{S9}$$

$$\hat{\theta}_{\mathrm{opt}}(k) = \hat{\theta}_{\mathrm{opt}}(k-1) - P(k)\gamma^{\mathrm{T}}(k)\bar{R}\psi(k), \tag{S10}$$

where

$$\beta(k) \triangleq [\bar{R}^{-1} + \gamma(k)P(k-1)\gamma^{\mathrm{T}}(k)]^{-1}, \tag{S11}$$

$$\gamma(k) \triangleq \begin{bmatrix} N\bar{\Phi}(k) \\ \Phi(k) \end{bmatrix}, \quad \bar{R} \triangleq \begin{bmatrix} R_z & 0_{l_z \times l_u} \\ 0_{l_u \times l_z} & \bar{R}_u \end{bmatrix}, \tag{S12}$$

$$\psi(k) \triangleq \begin{bmatrix} N\bar{\Phi}(k)\hat{\theta}_{\mathrm{opt}}(k-1) + z(k) - N\bar{U}(k) \\ \Phi(k)\hat{\theta}_{\mathrm{opt}}(k-1) \end{bmatrix}. \tag{S13}$$

The implemented control at step $k+1$ is given by

solution of (1)–(4) determines the state update and effective impulse response.

ADAPTIVE CONTROL ALGORITHM

Despite the fact that the model in (1)–(4) is a nonlinear, time-varying plant, RCAC uses extremely limited information to update the controller coefficients. Furthermore, no explicit information about the nonlinearity or time variation is used to select the adaptive tuning weights. The goal of this study was to determine the extent to which RCAC can accommodate the unmodeled features of (1)–(4). For SISO linear plants, RCAC requires limited modeling data, namely, the sign of the leading numerator coefficient, the relative degree, and the locations of NMP zeros, if any. This information is used to construct the filter G_{f}, which is used to compute the retrospective performance variable. As explained in [32], G_{f} serves as a target model for the closed-loop intercalated transfer function from the virtual control input perturbation to the performance variable. For application to IEEE13NTF, the RCAC tuning weights are chosen based on a combination of NST and PST.

At each step k, RCAC updates the feedback controller $G_{\mathrm{c},k}$ to optimally fit the intercalated transfer function to the target model G_{f}. The input of $G_{\mathrm{c},k}$ is the three voltage magnitude errors and three voltage angle errors at the performance node. Its output is the three active powers and three reactive powers extracted at the actuation node. The controller order and structure are chosen by the user, as are the adaptation weight R_θ, control weight R_u, and

$$u(k+1) = \Phi(k+1)\hat{\theta}_{\text{opt}}(k) = \Phi(k+1)\theta(k+1), \tag{S14}$$

where

$$\theta(k+1) \triangleq \hat{\theta}_{\text{opt}}(k). \tag{S15}$$

$\hat{\theta}_{\text{opt}}(0) = 0$ is initialized to reflect the absence of additional prior modeling information, and $\bar{R}_u = R_u I_{l_u}$ and $\bar{R}_\theta = R_\theta I_{l_\theta}$ are used where R_u and R_θ are scalar weightings.

FIXED-STRUCTURE CONTROLLER PARAMETERIZATION

Define the dynamic compensator of the form

$$u(k) = G_{\text{c},k}(\mathbf{q})y(k), \tag{S16}$$

$$G_{\text{c},k} \triangleq \begin{bmatrix} G_{\text{c},11,k} & \cdots & G_{\text{c},1l_y,k} \\ \vdots & \ddots & \vdots \\ G_{\text{c},l_u1,k} & \cdots & G_{\text{c},l_ul_y,k} \end{bmatrix}, \tag{S17}$$

where each entry $G_{\text{c},ij,k}$ of the $l_u \times l_y$ discrete-time transfer function $G_{\text{c},k}(\mathbf{q})$ is either an infinite-impulse-response (IIR) controller of a specified order ℓ_{ij} or a proportional-integral (PI) controller. That is,

$$G_{\text{c},ij,k}(\mathbf{q}) = \begin{cases} \dfrac{q_{ij,1}(k)\mathbf{q}^{\ell_{ij}-1} + \cdots + q_{ij,\ell_{ij}}(k)}{\mathbf{q}^{\ell_{ij}} - p_{ij,1}(k)\mathbf{q}^{\ell_{ij}-1} - \cdots - p_{ij,\ell_{ij}}(k)}, & \text{IIR}, \\ \dfrac{q_{ij,1}(k)}{\mathbf{q}} + \dfrac{q_{ij,2}(k)}{\mathbf{q}-1}, & \text{PI}. \end{cases} \tag{S18}$$

To construct $\theta(k)$, first define

$$\theta_{ij}(k) \triangleq \begin{cases} \begin{bmatrix} p_{ij,1}(k) \\ \vdots \\ p_{ij,\ell_{c,ij}}(k) \\ q_{ij,1}(k) \\ \vdots \\ q_{ij,\ell_{c,ij}}(k) \end{bmatrix} \in \mathbb{R}^{l_{\theta,ij}}, & \text{IIR } G_{\text{c},ij,k}, \\ \begin{bmatrix} q_{ij,1}(k) \\ q_{ij,2}(k) \end{bmatrix} \in \mathbb{R}^2, & \text{PI } G_{\text{c},ij,k}, \end{cases} \tag{S19}$$

which, in turn, are used to define

$$\theta_i(k) \triangleq \begin{bmatrix} \theta_{i1} \\ \vdots \\ \theta_{il_y} \end{bmatrix} \in \mathbb{R}^{l_{\theta_i}}, \tag{S20}$$

and, finally, define

$$\theta(k) \triangleq \begin{bmatrix} \theta_1 \\ \vdots \\ \theta_{l_u} \end{bmatrix} \in \mathbb{R}^{l_\theta}, \tag{S21}$$

where

$$l_{\theta,ij} = \begin{cases} 2\ell_{\text{c},ij}, & \text{IIR } G_{\text{c},ij,k}, \\ 2, & \text{PI } G_{\text{c},ij,k}, \end{cases} \tag{S22}$$

$$l_{\theta_i} \triangleq \sum_{j=1}^{l_y} l_{\theta,ij}, \quad l_\theta \triangleq \sum_{i=1}^{l_u}\sum_{j=1}^{l_y} l_{\theta,ij}. \tag{S23}$$

For each controller entry $G_{\text{c},ij,k}$, define

$$u_{ij}(k) \triangleq G_{\text{c},ij,k}(\mathbf{q})y_j(k), \tag{S24}$$

and construct $\phi_{ij}(k)$. For an IIR $G_{\text{c},ij,k}$ of order ℓ_{ij},

$$\phi_{ij}(k) \triangleq \begin{bmatrix} u_{ij}(k-1) \\ \vdots \\ u_{ij}(k-\ell_{ij}) \\ y_j(k-1) \\ \vdots \\ y_j(k-\ell_{ij}) \end{bmatrix}^T \in \mathbb{R}^{1\times l_{\theta,ij}}, \tag{S25}$$

and for a PI $G_{\text{c},ij,k}$,

$$\phi_{ij}(k) \triangleq \begin{bmatrix} y_j(k-1) \\ \sum_{p=0}^{k-1} y_j(p) \end{bmatrix}^T \in \mathbb{R}^{1\times l_{\theta,ij}}. \tag{S26}$$

Using $\phi_{ij}(k)$, construct

$$\phi_i(k) \triangleq [\phi_{i1} \ \cdots \ \phi_{il_y}] \in \mathbb{R}^{1\times l_{\theta_i}}, \tag{S27}$$

which in turn is used to construct

$$\Phi(k) \triangleq \text{diag}(\phi_1(k), \ldots, \phi_{l_u}(k)) \in \mathbb{R}^{l_u \times l_\theta}. \tag{S28}$$

cost weight R_z. The coefficients of $G_{\text{c},k}$ are entries of the controller coefficient vector $\theta(k)$. As in [32], the initial value $\theta(0)$ of $\theta(k)$ is set to zero for all simulations. This assumption reflects the absence of additional modeling information. In practice, $\theta(0)$ can be chosen to be nonzero based on modeling or prior adaptation. Details of RCAC and its implementation using recursive least squares to update θ are given in [32]. A summary of the algorithm is presented in "Fixed-Structure Retrospective Cost Adaptive Control Algorithm."

PROBLEM SETUP

Consider IEEE13NTF from Figure 1 (which is simulated with OpalRT RT-LAB, version 2017.0.4.59) and use the fixed-structure RCAC described in "Fixed-Structure Retrospective Cost Adaptive Control Algorithm" with a sparse target model G_f. RCAC is updated at 100 Hz, which is sufficiently fast for the time-varying load and PV-generation dynamics considered in this study. In this article, real customer PV-generation data are obtained from Pecan Street [36] and integrated into IEEE13NTF. In what follows, continuous time t and the sampled time step k are related by $t = k/100$.

In this article, only three phase performance nodes for command-following are considered. Specifically, for each performance node, define

$$y_0(k) \triangleq \begin{bmatrix} y_{0,\text{mag}}(k) \\ y_{0,\text{ang}}(k) \end{bmatrix}, \quad z(k) \triangleq \begin{bmatrix} z_{\text{mag}}(k) \\ z_{\text{ang}}(k) \end{bmatrix}, \tag{5}$$

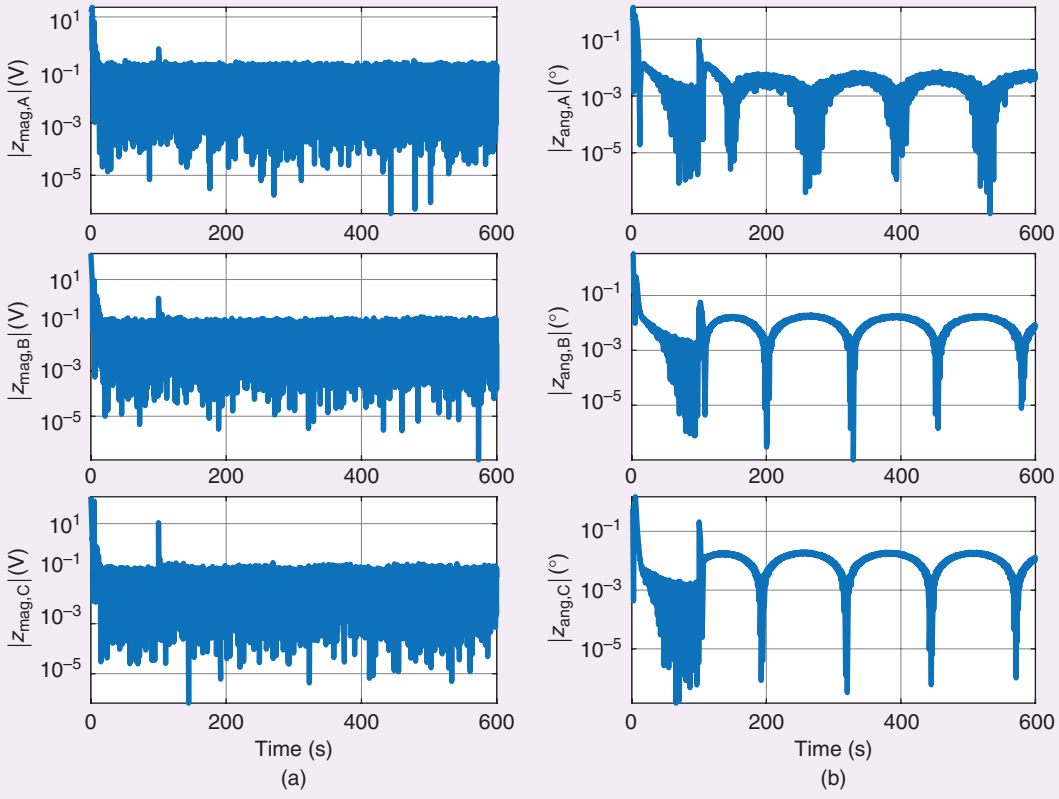

FIGURE 4 Nominal simulation tuning: the (a) voltage-magnitude error $|z_{mag}|$ and (b) voltage angle-magnitude error $|z_{ang}|$ at node 671 are shown on a logarithmic scale. Asymptotically, the voltage-magnitude and voltage-angle errors are approximately lower than 0.1 V and 0.01°, respectively.

where

$$y_{0,\mathrm{mag}}(k) \triangleq \begin{bmatrix} V_{\mathrm{mag,A}}(k) \\ V_{\mathrm{mag,B}}(k) \\ V_{\mathrm{mag,C}}(k) \end{bmatrix}, \qquad y_{0,\mathrm{ang}}(k) \triangleq \begin{bmatrix} V_{\mathrm{ang,A}}(k) \\ V_{\mathrm{ang,B}}(k) \\ V_{\mathrm{ang,C}}(k) \end{bmatrix}, \tag{6}$$

$$z_{\mathrm{mag}}(k) \triangleq \begin{bmatrix} z_{\mathrm{mag,A}}(k) \\ z_{\mathrm{mag,B}}(k) \\ z_{\mathrm{mag,C}}(k) \end{bmatrix}, \qquad z_{\mathrm{ang}}(k) \triangleq \begin{bmatrix} z_{\mathrm{ang,A}}(k) \\ z_{\mathrm{ang,B}}(k) \\ z_{\mathrm{ang,C}}(k) \end{bmatrix}. \tag{7}$$

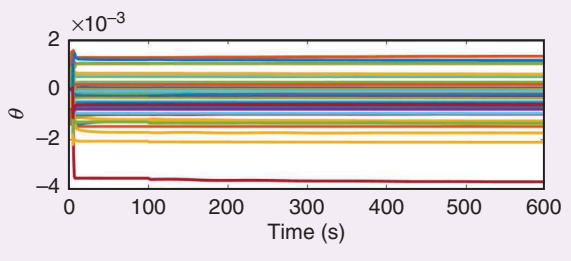

FIGURE 5 Nominal simulation tuning: the retrospective cost adaptive control (RCAC) controller $G_{c,k}$ adapts to follow the setpoint commands. RCAC readapts at $t = 5$ s to account for the step-load disturbance and again at $t = 100$ s to account for the additional harmonic component of the load disturbance.

Phasor-based control is set up as a servo problem, as shown in Figure 2, with the objective being phase balancing. Consequently, r has the same dimensions as y_0 and is defined as

$$r(k) \triangleq \begin{bmatrix} r_{\mathrm{mag}} \\ r_{\mathrm{mag}} \\ r_{\mathrm{mag}} \\ r_{\mathrm{ang}} \\ r_{\mathrm{ang}} - 120^\circ \\ r_{\mathrm{ang}} + 120^\circ \end{bmatrix}, \tag{8}$$

which allows for specification of the command for each node as a pair of two scalars $r_{\mathrm{mag}}, r_{\mathrm{ang}}$ instead of six scalars. This reference is designed to balance the three phases.

Actuators are modeled as idealized three-phase, four-quadrant operation dc/ac inverters, which are connected to infinitely large battery packs at the actuation nodes. To avoid the case in which an actuation node goes offline, we assume that each battery pack has infinite capacity. Each RCAC controller commands a single inverter, which can add or extract active and reactive power at each of the three phases. The output $u(k)$ of the controller $G_{c,k}$ at step k is defined to be $u(k)$, scaled by a fixed scaling. An effective scaling is determined from the simulated closed-loop response. Specifically, the power extracted at an actuation node is given by

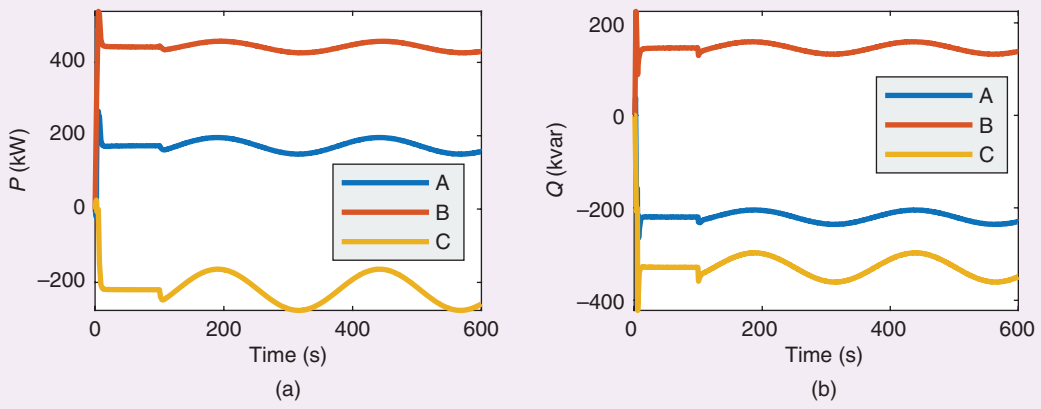

FIGURE 6 Nominal simulation tuning: the (a) active and (b) reactive power extracted from each phase by the retrospective cost adaptive control controller $G_{c,k}$ at node 675 is shown.

$$P_{\text{act}}(k) \triangleq \begin{bmatrix} P_{\text{act},A}(k) \\ Q_{\text{act},A}(k) \\ P_{\text{act},B}(k) \\ Q_{\text{act},B}(k) \\ P_{\text{act},C}(k) \\ Q_{\text{act},C}(k) \end{bmatrix} = 200u(k). \tag{9}$$

Since only three-phase performance and actuation nodes are considered, it follows that $l_u = l_y = 6$ for all simulations. Additionally, define

$$v(k) \triangleq \begin{bmatrix} v_{\text{mag}}(k) \\ v_{\text{ang}}(k) \end{bmatrix}, \tag{10}$$

$$v_{\text{mag}}(k) \triangleq \begin{bmatrix} v_{\text{mag},A}(k) \\ v_{\text{mag},B}(k) \\ v_{\text{mag},C}(k) \end{bmatrix}, \quad v_{\text{ang}}(k) \triangleq \begin{bmatrix} v_{\text{ang},A}(k) \\ v_{\text{ang},B}(k) \\ v_{\text{ang},C}(k) \end{bmatrix}, \tag{11}$$

where each component of $v_{\text{mag}}(k)$ is Gaussian white noise with standard deviation 0.05 V, and each component of $v_{\text{ang}}(k)$ is Gaussian white noise with standard deviation 0.0005°.

NOMINAL SIMULATION TUNING

In this section, the controller structure, weightings, and target model are determined by running multiple simulations of a single scenario. The scenario selected for NST is command-following at node 671, with load disturbances at nodes 611 and 634 and actuation at node 675 (Figure 3).

Define the active and reactive power extracted at node 634 as

$$\begin{bmatrix} P_{634,A}(k) \\ Q_{634,A}(k) \\ P_{634,B}(k) \\ Q_{634,B}(k) \\ P_{634,C}(k) \\ Q_{634,C}(k) \end{bmatrix} = (1 + d(k)) \begin{bmatrix} 160\ \text{kW} \\ 110\ \text{kvar} \\ 120\ \text{kW} \\ 90\ \text{kvar} \\ 120\ \text{kW} \\ 90\ \text{kvar} \end{bmatrix}, \tag{12}$$

the active and reactive power extracted at node 611 as

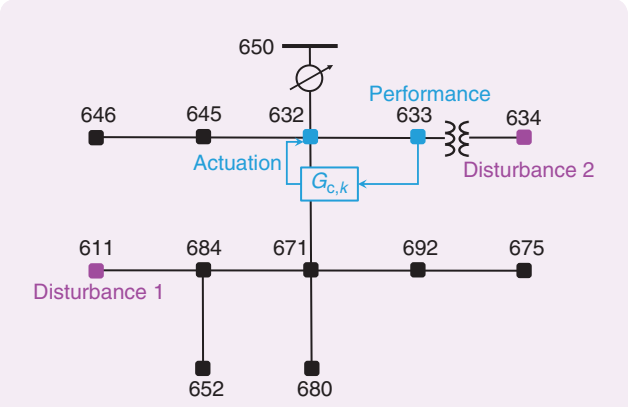

FIGURE 7 Perturbed simulation testing 1: at node 632, the controller $G_{c,k}$ can add or remove active and reactive power. At node 633, the controller $G_{c,k}$ has access to the voltage magnitude and angle measurements, where the voltage angles are relative to the slack bus at node 650. At nodes 611 and 634, the active and reactive power is varied, which represents an unmodeled load disturbance.

$$\begin{bmatrix} P_{611}(k) \\ Q_{611}(k) \end{bmatrix} = (1 + d(k)) \begin{bmatrix} 170\ \text{kW} \\ 80\ \text{kvar} \end{bmatrix}, \tag{13}$$

and the time-varying load disturbance $d(k)$ as

$$d(k) = \begin{cases} 0, & k < 500, \\ 1, & 500 \le k < 10000, \\ 1 + \dfrac{\sin 0.00025k}{4}, & k \ge 10000, \end{cases} \tag{14}$$

and set

$$r_{\text{mag}}(k) = 2267\ V \tag{15}$$

$$r_{\text{ang}}(k) = -5.3°. \tag{16}$$

To simplify the MIMO controller, each SISO entry of the MIMO controller is chosen to be either PI or second-order IIR. Based on simulation (5), the 6×6 controller structure

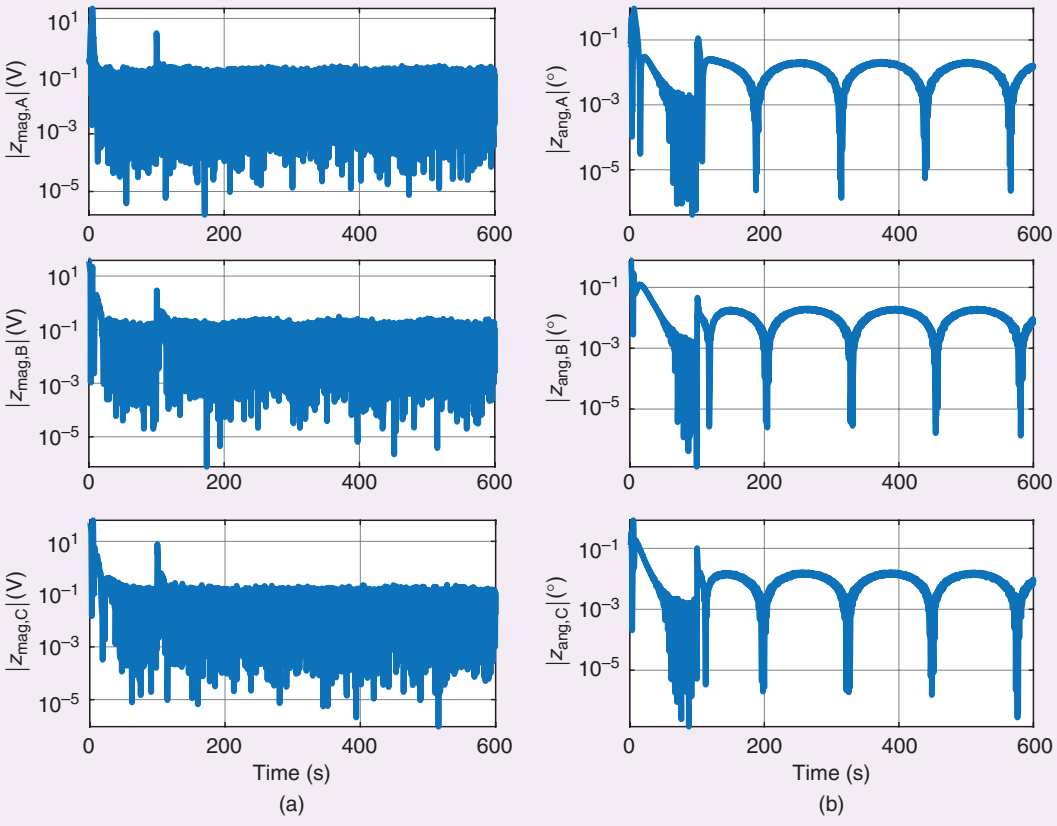

FIGURE 8 Perturbed simulation testing 1: the (a) voltage-magnitude error $|z_{mag}|$ and (b) voltage angle-magnitude error $|z_{ang}|$ at node 633 are shown on a logarithmic scale. Asymptotically, the voltage-magnitude and voltage-angle errors are approximately lower than 0.1 V and 0.01°, respectively.

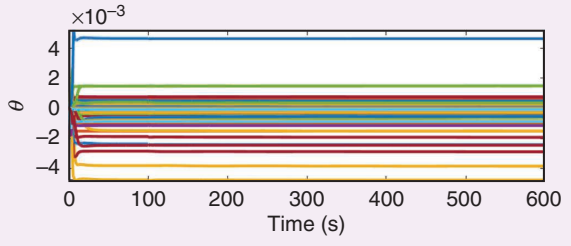

FIGURE 9 Perturbed simulation testing 1: the retrospective cost adaptive control (RCAC) controller $G_{c,k}$ adapts to follow the set-point commands. RCAC readapts at $t = 5$ s to account for the step-load disturbance and again at $t = 100$ s to account for the additional harmonic component of the load disturbance.

with the least complexity that follows phase-balancing commands is given by

$$\begin{bmatrix} \text{PI} & \text{IIR} & \text{PI} & \text{PI} & \text{PI} & \text{PI} \\ \text{PI} & \text{PI} & \text{PI} & \text{IIR} & \text{PI} & \text{PI} \\ \text{PI} & \text{PI} & \text{PI} & \text{PI} & \text{PI} & \text{IIR} \\ \text{IIR} & \text{PI} & \text{PI} & \text{PI} & \text{PI} & \text{PI} \\ \text{PI} & \text{PI} & \text{IIR} & \text{PI} & \text{PI} & \text{PI} \\ \text{PI} & \text{PI} & \text{PI} & \text{PI} & \text{IIR} & \text{PI} \end{bmatrix}. \tag{17}$$

Fixed-structure RCAC, described in "Fixed-Structure Retrospective Cost Adaptive Control Algorithm," is used to adapt the controller coefficients. For (17), RCAC adapts 84 coefficients. If each entry of (17) were chosen to be second-order IIR, then RCAC would need to adapt 144 coefficients.

Additionally, set $R_\theta = 10^{-9}$, $R_u = 0$, and $R_z = \text{diag}(1, 1, 1, 100, 100, 100)$ and use $G_f(\mathbf{q}) = (1/\mathbf{q})\hat{H}_1$, where $\hat{H}_1$ is constructed by the following procedure:

1) First, obtain H_1 by impulsing each input at the actuation node in IEEE13NTF at the initial conditions and recording the first value of each measurement at the performance node. Separately replace each entry of H_1 with zero, and record the entries whose replacement by zero does not cause RCAC to fail. These entries are highlighted in bold:

$$\begin{bmatrix} \mathbf{92.54} & 67.93 & \mathbf{6.71} & \mathbf{-8.39} & \mathbf{-48.21} & \mathbf{-3.84} \\ \mathbf{-89.25} & \mathbf{-3.81} & \mathbf{9.81} & 20.64 & \mathbf{14.38} & \mathbf{-28.56} \\ \mathbf{24.75} & \mathbf{-26.95} & \mathbf{-9.35} & \mathbf{-0.12} & \mathbf{58.68} & 83.23 \\ 4.03 & \mathbf{-0.50} & \mathbf{-0.18} & \mathbf{-0.15} & \mathbf{0.07} & \mathbf{0.87} \\ \mathbf{0.12} & \mathbf{0.77} & 0.48 & \mathbf{-0.20} & \mathbf{-0.97} & \mathbf{-0.47} \\ -1.74 & -0.52 & \mathbf{-0.07} & \mathbf{0.15} & 2.60 & -0.66 \end{bmatrix}.$$

2) Next, separately replace each entry of H_1 with its additive inverse, and record the entries for which

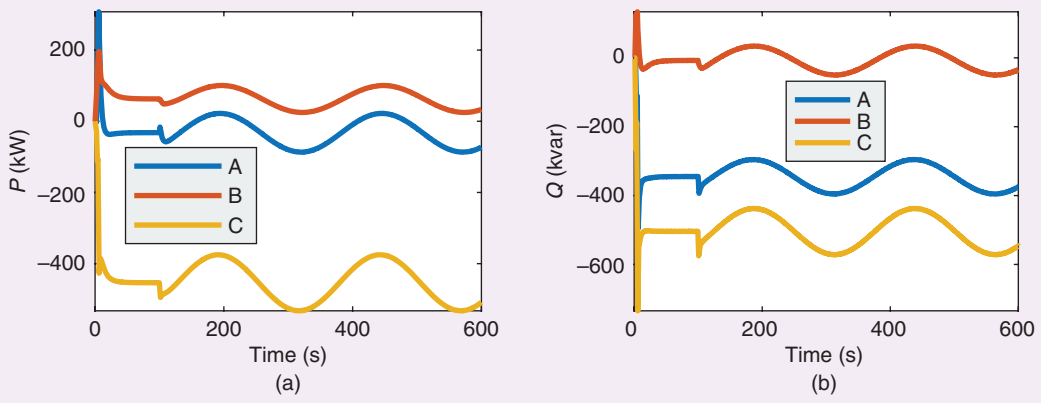

FIGURE 10 Perturbed simulation testing 1: the (a) active and (b) reactive power extracted from each phase by the retrospective cost adaptive control controller $G_{c,k}$ at node 632 is shown.

replacement by the additive inverse does not cause RCAC to fail. These entries are highlighted in bold:

$$\begin{bmatrix} \mathbf{92.54} & 67.93 & 6.71 & \mathbf{-8.39} & \mathbf{-48.21} & \mathbf{-3.84} \\ \mathbf{-89.25} & \mathbf{-3.81} & \mathbf{9.81} & 20.64 & \mathbf{14.38} & \mathbf{-28.56} \\ \mathbf{24.75} & -26.95 & -9.35 & \mathbf{-0.12} & \mathbf{58.68} & 83.23 \\ 4.03 & \mathbf{-0.50} & \mathbf{-0.18} & \mathbf{-0.15} & \mathbf{0.07} & \mathbf{0.87} \\ \mathbf{0.12} & \mathbf{0.77} & 0.48 & \mathbf{-0.20} & \mathbf{-0.97} & \mathbf{-0.47} \\ \mathbf{-1.74} & \mathbf{-0.52} & \mathbf{-0.07} & \mathbf{0.15} & 2.60 & -0.66 \end{bmatrix}.$$

3) Replace all 29 of the bold entries in steps 1 and 2 with zero, which yields

$$\begin{bmatrix} 0 & 67.93 & 0 & 0 & 0 & 0 \\ 0 & 0 & 0 & 20.64 & 0 & 0 \\ 0 & 0 & 0 & 0 & 0 & 83.23 \\ 4.03 & 0 & 0 & 0 & 0 & 0 \\ 0 & 0 & 0.48 & 0 & 0 & 0 \\ 0 & 0 & 0 & 0 & 2.60 & -0.66 \end{bmatrix}.$$

4) Next, separately replace each nonzero entry in $\hat{H}_1$ constructed in the previous step with zero to determine the modified matrix $\hat{H}_1$ that has the smallest number of nonzero entries for which RCAC does not fail, which is given by

$$\begin{bmatrix} 0 & 67.93 & 0 & 0 & 0 & 0 \\ 0 & 0 & 0 & 20.64 & 0 & 0 \\ 0 & 0 & 0 & 0 & 0 & 83.23 \\ 4.03 & 0 & 0 & 0 & 0 & 0 \\ 0 & 0 & 0.48 & 0 & 0 & 0 \\ 0 & 0 & 0 & 0 & 2.60 & 0 \end{bmatrix}. \tag{18}$$

5) Finally, the numerical values in (18) suggest that it may be possible to parameterize (18) by using only two numbers. Numerical testing suggests 200 V for magnitude and 5° for angle, which yields

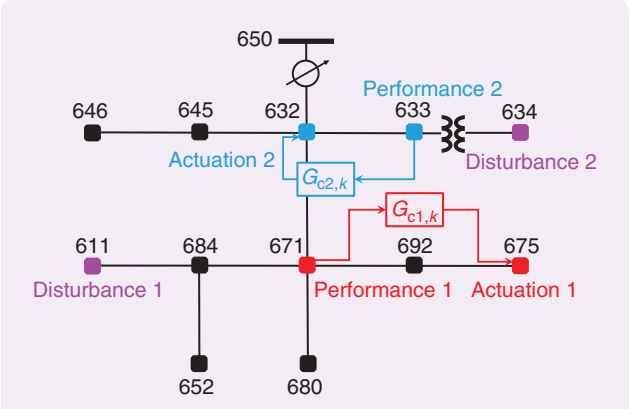

FIGURE 11 Perturbed simulation testing 2: at node 675, subcontroller $G_{c1,k}$ can add or remove active and reactive power. At node 671, subcontroller $G_{c1,k}$ has access to the voltage magnitude and angle measurements, where the voltage angles are relative to the slack bus at node 650. At node 632, subcontroller $G_{c2,k}$ can add or remove active and reactive power. At node 633, subcontroller $G_{c2,k}$ has access to the voltage magnitude and angle measurements, where the voltage angles are relative to the slack bus at node 650. At nodes 611 and 634, the active and reactive power is varied to represent an unmodeled load disturbance.

$$\hat{H}_1 = \begin{bmatrix} 0 & 200 & 0 & 0 & 0 & 0 \\ 0 & 0 & 0 & 200 & 0 & 0 \\ 0 & 0 & 0 & 0 & 0 & 200 \\ 5 & 0 & 0 & 0 & 0 & 0 \\ 0 & 0 & 5 & 0 & 0 & 0 \\ 0 & 0 & 0 & 0 & 5 & 0 \end{bmatrix}. \tag{19}$$

Note that the rows of (19) can be rearranged to construct a 6×6 diagonal matrix. This rearrangement yields a specific pairing of the input and output variables in (5)–(7). Figures 4–6 illustrate RCAC using (19), the controller structure (17), and the chosen weightings, with voltage magnitude and angle commands at node 671, actuation at

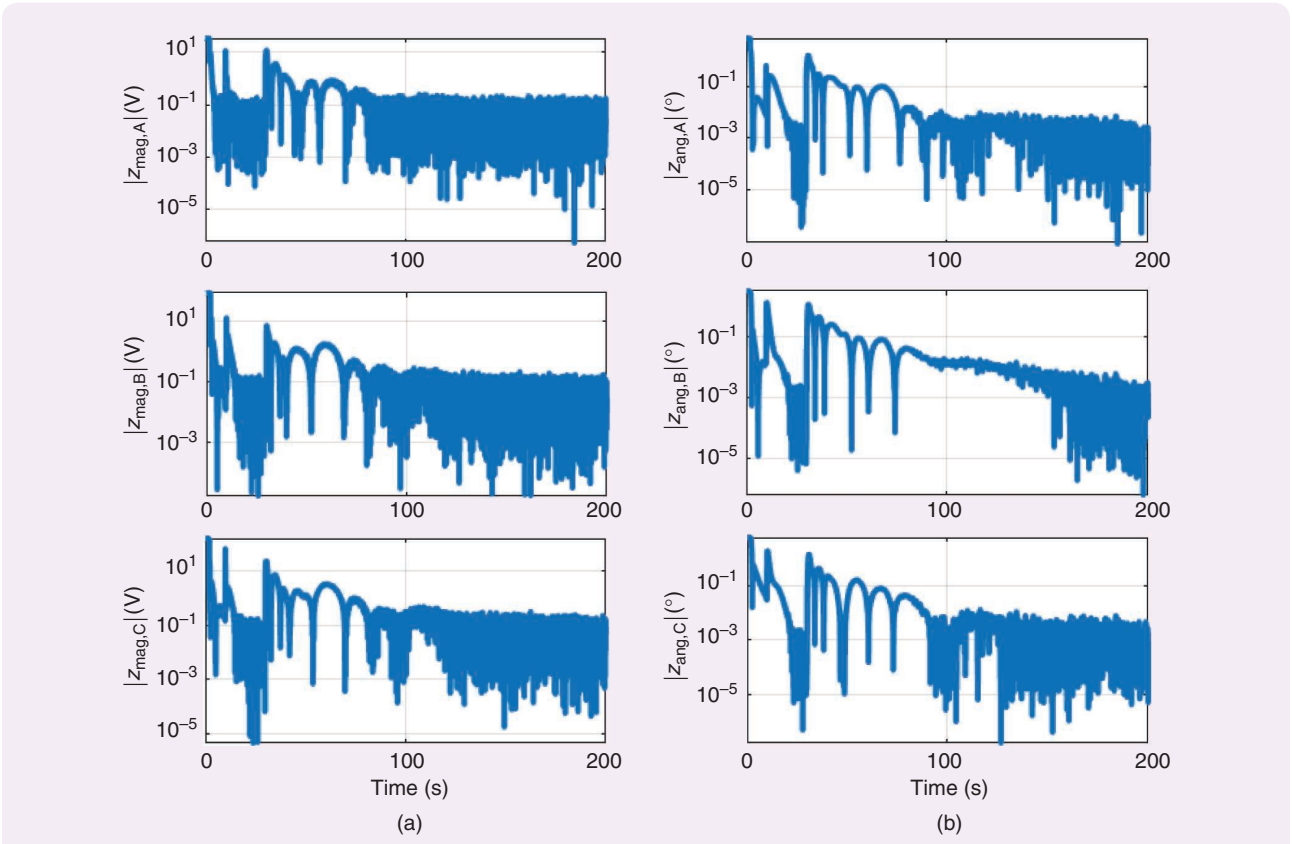

FIGURE 12 Perturbed simulation testing 2: the (a) voltage-magnitude error $|z_{mag}|$ and (b) voltage angle-magnitude error $|z_{ang}|$ at node 671 are shown on a logarithmic scale. Asymptotically, the voltage-magnitude and voltage-angle errors are approximately lower than 0.1 V and 0.01°, respectively.

node 675, and the time-varying load disturbance (14) at nodes 611 and 634 in the presence of the sensor noise (34). This completes the NST.

Perturbed Simulation Testing

In this section, the controller structure, weightings, and target model obtained by NST in the previous section are applied to multiple scenarios involving perturbed simulations. Each simulation represents a perturbation of the nominal simulation in terms of the disturbance signals; actuator saturation levels; and choice of disturbance, actuation, and performance nodes. For all simulations, the controller structure given by (17) is used with the weightings $R_\theta = 10^{-9}$, $R_u = 0$, and $R_z = \mathrm{diag}(1, 1, 1, 100, 100, 100)$ and target model $G_f(\mathbf{q}) = (1/\mathbf{q})\hat{H}_1$, where $\hat{H}_1$ is given by (19). Each case is simulated once, and no attempt is made to retune RCAC based on the response of the closed-loop system.

Perturbed Simulation Testing 1 (PST 1)

PST 1 tests command-following at node 633, with load disturbance at nodes 611 and 634 and actuation at node 632 (Figure 7). The active and reactive power at nodes 634 and 611 is defined using (12) and (13), respectively, and the load disturbance $d(k)$ is set using (14). For node 633, the command is set as

$$r_{\mathrm{mag}}(k) = 2312 \text{ V}, \tag{20}$$

$$r_{\mathrm{ang}}(k) = -2.56°. \tag{21}$$

For the controller $G_{c,k}$, the tuning weights described at the beginning of this section are used. Feedback control with adaptation begins at $t = 2$ s. Figures 8–10 illustrate RCAC with voltage magnitude and angle commands at node 633, actuation at node 632, and the time-varying load disturbance (14) at nodes 611 and 634 in the presence of the sensor noise (34). ◊

Perturbed Simulation Testing 2 (PST 2)

PST 2 tests command-following at nodes 671 and 633, with load disturbances at nodes 611 and 634 and actuation at nodes 675 and 632, using decentralized control (Figure 11). The active and reactive power at nodes 634 and 611 is defined using (12) and (13), respectively, and the load disturbance $d(k)$ is set as

$$d(k) = \begin{cases} 0, & k < 1{,}000, \\ 1, & \text{otherwise.} \end{cases} \tag{22}$$

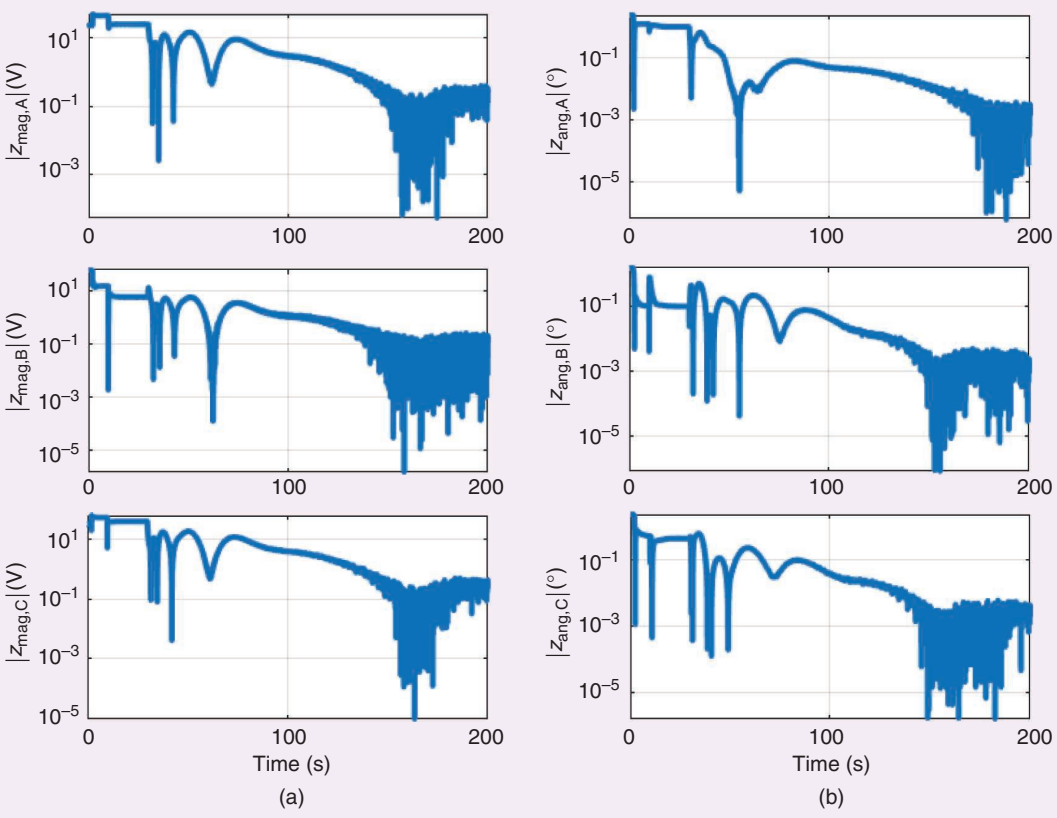

FIGURE 13 Perturbed simulation testing 2: the (a) voltage-magnitude error $|z_{mag}|$ and (b) voltage angle-magnitude error $|z_{ang}|$ for node 633 are shown on a logarithmic scale. Asymptotically, the voltage-magnitude and voltage-angle errors are approximately lower than 0.1 V and 0.01°, respectively.

For node 671, the command is set as

$$r_{671,\mathrm{mag}}(k) = 2{,}300 \text{ V}, \tag{23}$$

$$r_{671,\mathrm{ang}}(k) = 1.23°, \tag{24}$$

and for node 633, the command is set as

$$r_{633,\mathrm{mag}}(k) = 2290 \text{ V}, \tag{25}$$

$$r_{633,\mathrm{ang}}(k) = -0.34°. \tag{26}$$

For each subcontroller $G_{c1,k}$ and $G_{c2,k}$, the tuning weights described at the beginning of this section are used. Feedback control with adaptation using subcontrollers $G_{c1,k}$ and $G_{c2,k}$ begins at $t = 2$ s and $t = 30$ s, respectively. Figures 12–16 illustrate a pair of decentralized RCAC subcontrollers with voltage magnitude and angle commands at nodes 671 and 633, actuation at nodes 675 and 632, and the time-varying load disturbance (22) at nodes 611 and 634 in the presence of the sensor noise (34). There is no direct communication between subcontrollers $G_{c1,k}$ and $G_{c2,k}$. ♢

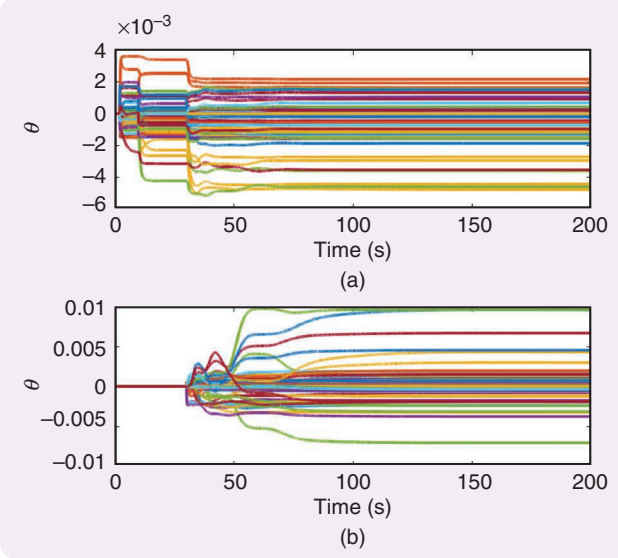

FIGURE 14 Perturbed simulation testing 2: (a) $\theta(k)$ for subcontroller $G_{c1,k}$ is zero for $t < 2$ s, after which the adaptation of subcontroller $G_{c1,k}$ begins to follow the setpoint commands. Subcontroller $G_{c1,k}$ readapts at $t = 10$ s to account for the step disturbance and again at $t = 30$ s to account for subcontroller $G_{c2,k}$ starting adaptation. (b) $\theta(k)$ for subcontroller $G_{c2,k}$ is zero for $t < 30$ s, after which adaptation of subcontroller $G_{c2,k}$ begins to follow the setpoint commands.

Perturbed Simulation Testing 3 (PST 3)

PST 3 tests command-following at node 671, with load disturbances at nodes 611 and 634 and actuation at nodes 675

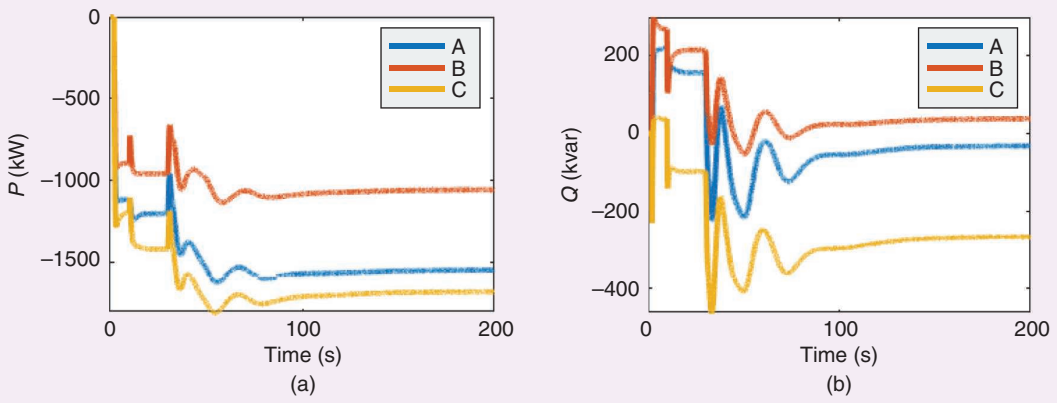

FIGURE 15 Perturbed simulation testing 2: the (a) active and (b) reactive power extracted by subcontroller $G_{c1,k}$ from each phase at node 675 is shown.

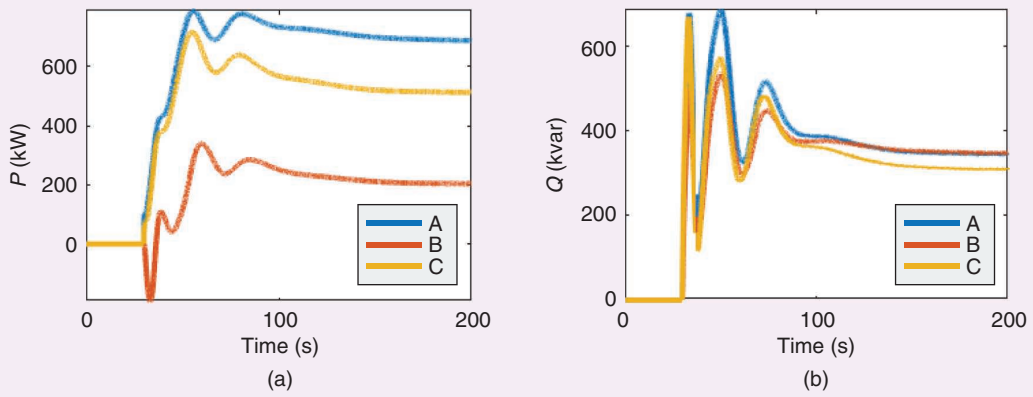

FIGURE 16 Perturbed simulation testing 2: the (a) active and (b) reactive power extracted by subcontroller $G_{c2,k}$ from each phase at node 632 is shown.

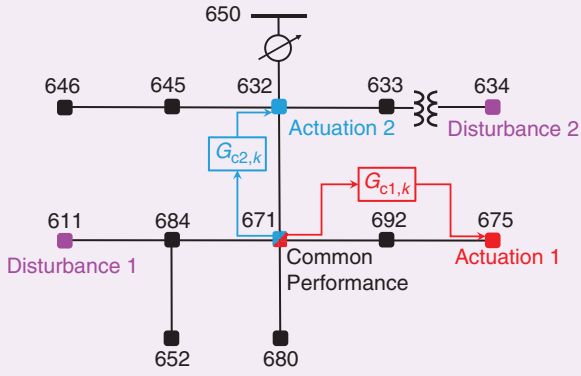

FIGURE 17 Perturbed simulation testing 3: at node 675 and node 632, subcontroller $G_{c1,k}$ and subcontroller $G_{c2,k}$ can add or remove active and reactive power, respectively. At node 671, subcontrollers $G_{c1,k}$ and $G_{c2,k}$ have access to the voltage magnitude and angle measurements, where the voltage angles are relative to the slack bus at node 650. At nodes 611 and 634, the active and reactive power is varied to represent an unmodeled load disturbance.

and 632 with unknown multivariable actuator saturation, using decentralized control (Figure 17). The active and reactive power at nodes 634 and 611 is defined using (12) and (13), respectively, and the load disturbance $d(k)$ is

$$d(k) = \begin{cases} 0, & k < 1000, \\ 1, & \text{otherwise.} \end{cases} \tag{27}$$

For node 671, the command is set as

$$r_{671,\text{mag}}(k) = 2267 \text{ V}, \tag{28}$$

$$r_{671,\text{ang}}(k) = -5.3°. \tag{29}$$

To simulate an unknown multivariable-actuator saturation at nodes 632 and 675, on each phase $i \in \{A, B, C\}$, set

$$P_{\text{act,i}} = \begin{cases} P_{\text{act,i,req}}, & P^2_{\text{act,i,req}} + Q^2_{\text{act,i,req}} \le S^2_{\max} \\ S_{\max} \cos\alpha, & \text{otherwise} \end{cases}, \tag{30}$$

$$Q_{\text{act,i}} = \begin{cases} Q_{\text{act,i,req}}, & P^2_{\text{act,i,req}} + Q^2_{\text{act,i,req}} \le S^2_{\max} \\ S_{\max} \sin\alpha, & \text{otherwise} \end{cases}, \tag{31}$$

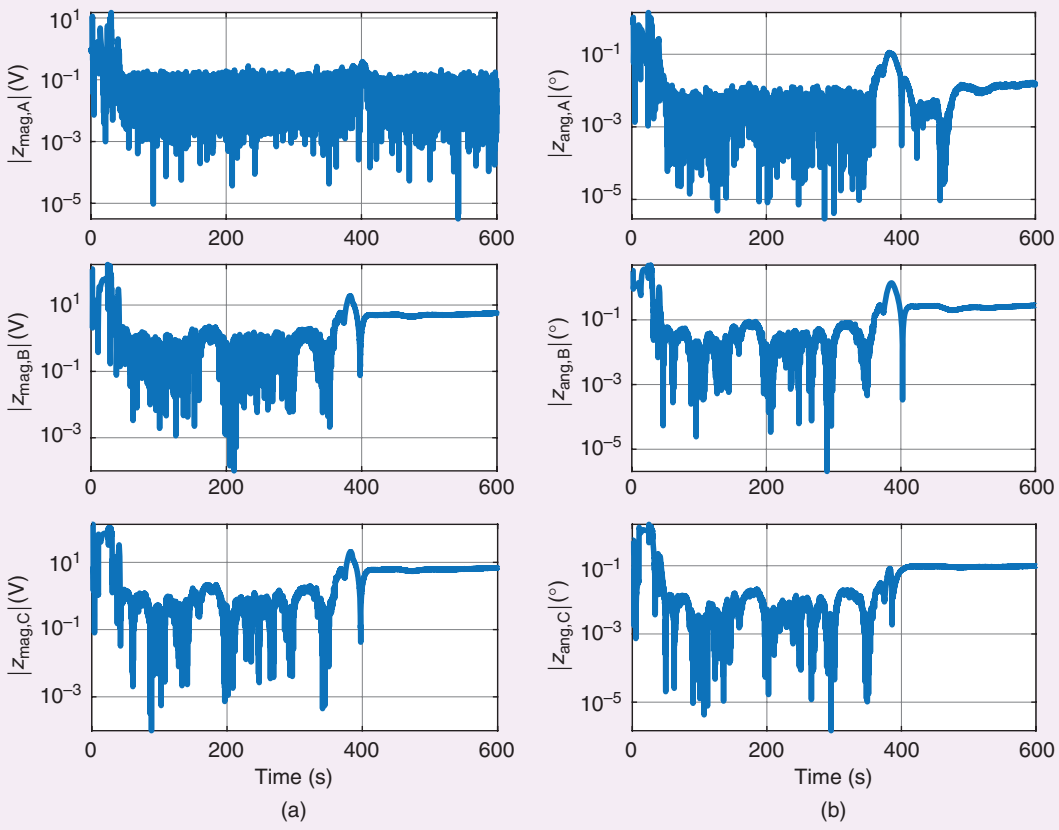

FIGURE 18 Perturbed simulation testing 3: the (a) voltage-magnitude error $|z_{mag}|$ and (b) voltage angle-magnitude error $|z_{ang}|$ for node 671 are shown on a logarithmic scale. Asymptotically, the voltage-magnitude and voltage-angle errors are approximately lower than 1 V and 0.1°, respectively.

where

$$\alpha \triangleq \operatorname{atan2}(Q_{\mathrm{act,i,req}}, P_{\mathrm{act,i,req}}). \tag{32}$$

$P_{\mathrm{act,i}}$ and $Q_{\mathrm{act,i}}$ are the active and reactive power extracted at phase i in kilowatts and kvar, respectively; $P_{\mathrm{act,i,req}}$ and $Q_{\mathrm{act,i,req}}$ are the requested active and reactive power extraction at phase i in kilowatts and kvar, respectively; $S_{\max} = 350$ kVA is the maximum apparent power rating for each phase of the inverter; and arguments of k are omitted for clarity. This saturation represents an upper limit on the apparent power extracted or injected at each phase: $S_{\max}$.

For each subcontroller $G_{c1,k}$ and $G_{c2,k}$, the tuning weights described at the beginning of this section are used. Feedback control with adaptation using subcontrollers $G_{c1,k}$ and $G_{c2,k}$ begins at $t = 2$ s and $t = 30$ s, respectively. Figures 18–21 illustrate a pair of decentralized RCAC subcontrollers with voltage magnitude and angle commands at node 671, actuation at nodes 675 and 632, and the time-varying load disturbance (27) at nodes 611 and 634 in the presence of the sensor noise (34). There is no direct communication between subcontrollers $G_{c1,k}$ and $G_{c2,k}$.

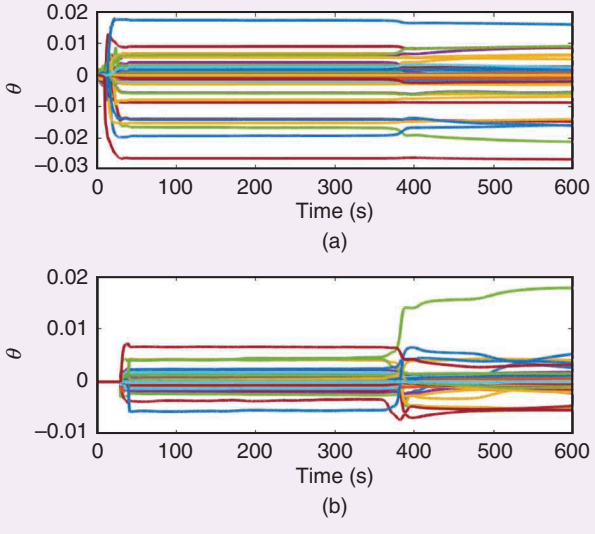

FIGURE 19 Perturbed simulation testing 3: (a) at $t = 2$ s, subcontroller $G_{c1,k}$ begins adapting, and (b) at $t = 30$ s, subcontroller $G_{c2,k}$ begins adapting. The retrospective cost adaptive control has no knowledge of the saturation.

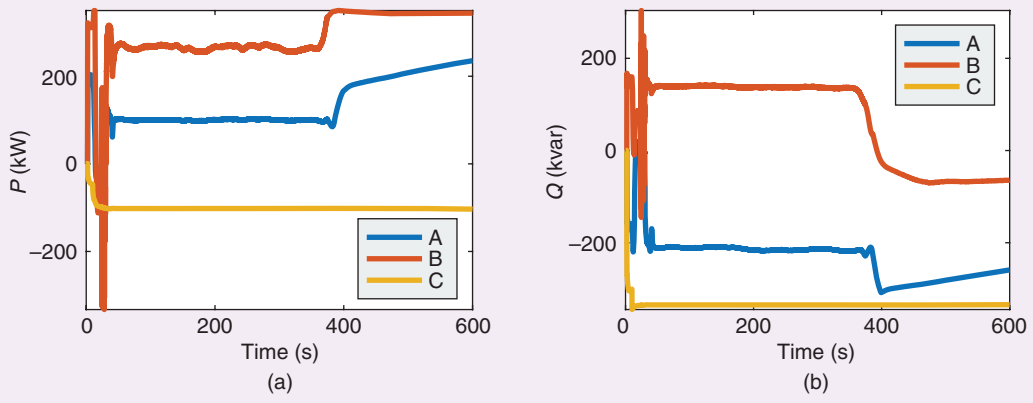

FIGURE 20 Perturbed simulation testing 3: the (a) active and (b) reactive power extracted by subcontroller $G_{c1,k}$ from each phase at node 675 is shown.

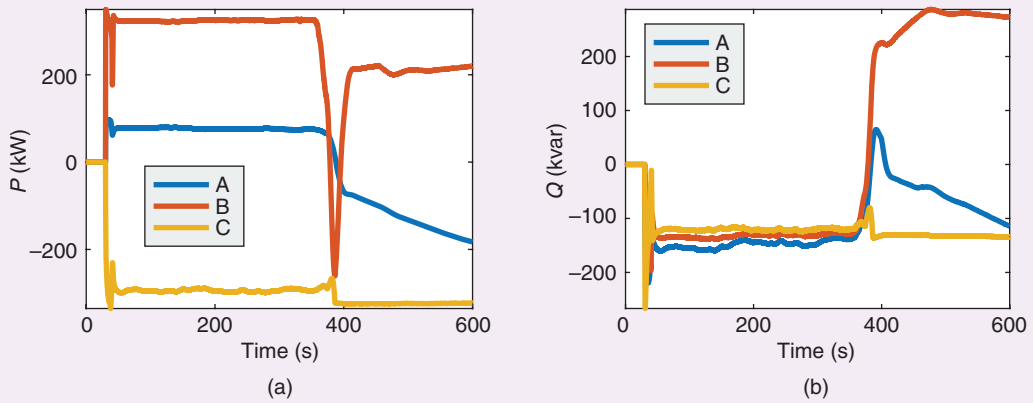

FIGURE 21 Perturbed simulation testing 3: the (a) active and (b) reactive power extracted by subcontroller $G_{c2,k}$ from each phase at node 632 is shown.

In Figure 22, the requested and extracted reactive power is plotted versus the requested and extracted active power for $0 \le k \le 60{,}000$ for each phase, *A*, *B*, *C*, at each actuation node. This shows that the unknown multivariable-actuator saturation affects five of the six phases of the two actuation nodes. RCAC has no knowledge of either the saturation form or level. ♢

Perturbed Simulation Testing 4 (PST4)

PST 4 tests command-following at node 671, with PV generation at nodes 611, 634, 645, 646, 652, and 692 and actuation at nodes 675 and 632, using decentralized control (Figure 23). PV penetration in IEEE13NTF is included by using the following procedure. From the Pecan Street online repository [36], 24 h of generation and consumption data (midnight to midnight) are obtained for 200 customers with PV generation capability. Since these data are per minute, linear interpolation is used to obtain subminute data for simulation. Next, for nodes 611, 634, 645, 646, 652, and 692, these data are aggregated using combinations of the 200 customers. The static loads in IEEE13NTF are then replaced at each PV node with the aggregated data. The aggregated data represent a collection of loads with a significant proportion of PV generation. The time-varying load is a disturbance to be rejected by RCAC. For node 671, the command is

$$r_{671,\mathrm{mag}}(k) = 2267 \text{ V}, \tag{33}$$

$$r_{671,\mathrm{ang}}(k) = -5.3°. \tag{34}$$

For each subcontroller $G_{c1,k}$ and $G_{c2,k}$, the tuning weights described at the beginning of this section are used. There is no communication between subcontrollers $G_{c1,k}$ and $G_{c2,k}$. Feedback control with adaptation using subcontrollers $G_{c1,k}$ and $G_{c2,k}$ begins at $t = 2$ s and $t = 30$ s, respectively. Figures 24–27 illustrate a pair of decentralized

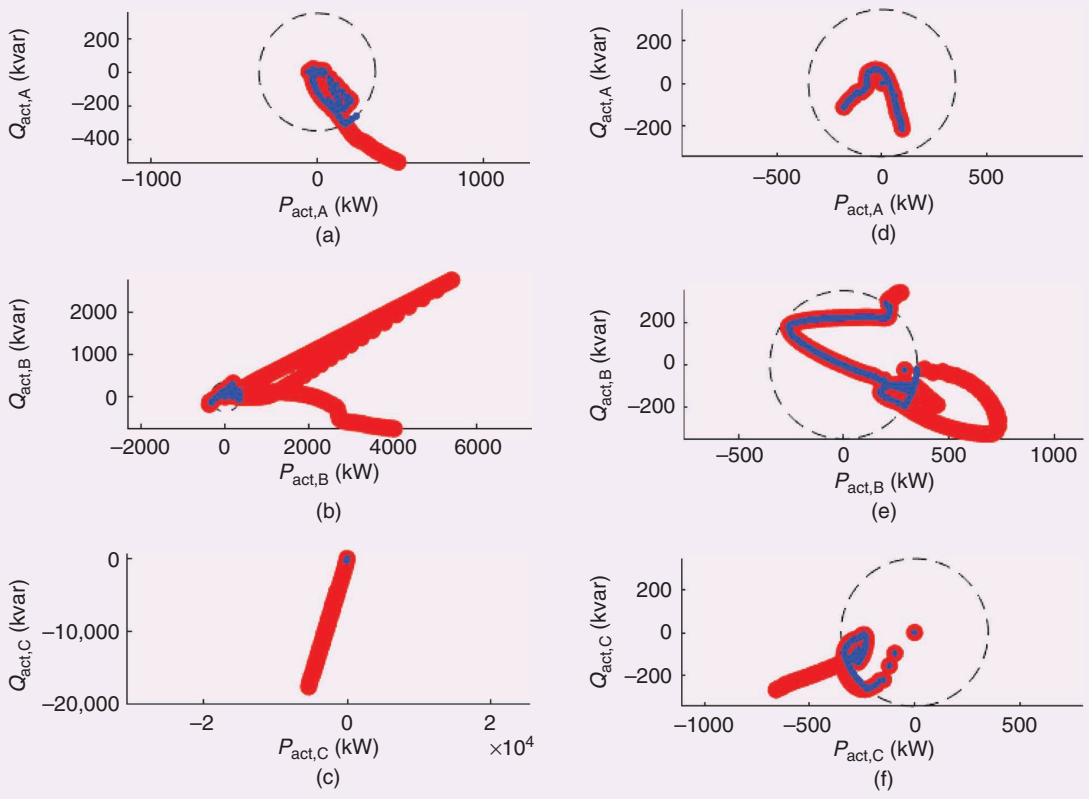

FIGURE 22 Perturbed simulation testing 3: the requested (red) and applied (blue) power of phases A, B, and C at node 675 is shown in (a), (b), and (c), respectively. The requested (red) and applied (blue) power of phases A, B, and C at node 632 is shown in (d), (e), and (f), respectively. The black, dashed circles represent the upper limit of apparent power flow in the actuator $S_{\max}$ defined in (30) and (31).

RCAC subcontrollers with voltage magnitude and angle commands at node 671, actuation at nodes 675 and 632, and PV generation at nodes 611, 634, 645, 646, 652, and 692 in the presence of the sensor noise (34). Define

$$\text{PV penetration} \triangleq \frac{\max_t G(t)}{\max_t L(t)} \times 100\%, \tag{35}$$

where $G(t)$ is the total PV generation across all nodes, and $L(t)$ is the total load across all nodes. For this simulation, PV penetration = 70.61%. ♢

CONCLUSIONS

This article provided a numerical investigation of phasor-based control of three-phase power using the IEEE13NTF model provided by the OPAL-RT RT-Lab ePHASORSIM package. Since the details of the ePHASORSIM implementation of IEEE13NTF are inaccessible, the IEEE13NTF model was treated as an opaque executable simulation, and controller tuning was based entirely on simulation. RCAC was applied to this system in two phases: NST and PST.

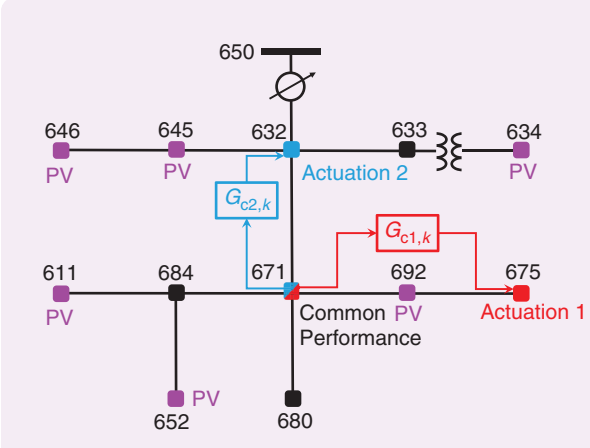

FIGURE 23 Perturbed simulation testing 4: at nodes 675 and 632, subcontrollers $G_{c1,k}$ and $G_{c2,k}$ can add or remove active and reactive power, respectively. At node 671, subcontrollers $G_{c1,k}$ and $G_{c2,k}$ have access to the voltage magnitude and angle measurements, where the voltage angles are relative to the slack bus at node 650. Nodes 611, 634, 645, 646, 652, and 692 emulate diurnal photovoltaic (PV) power generation and consumption to represent unmodeled load disturbances.

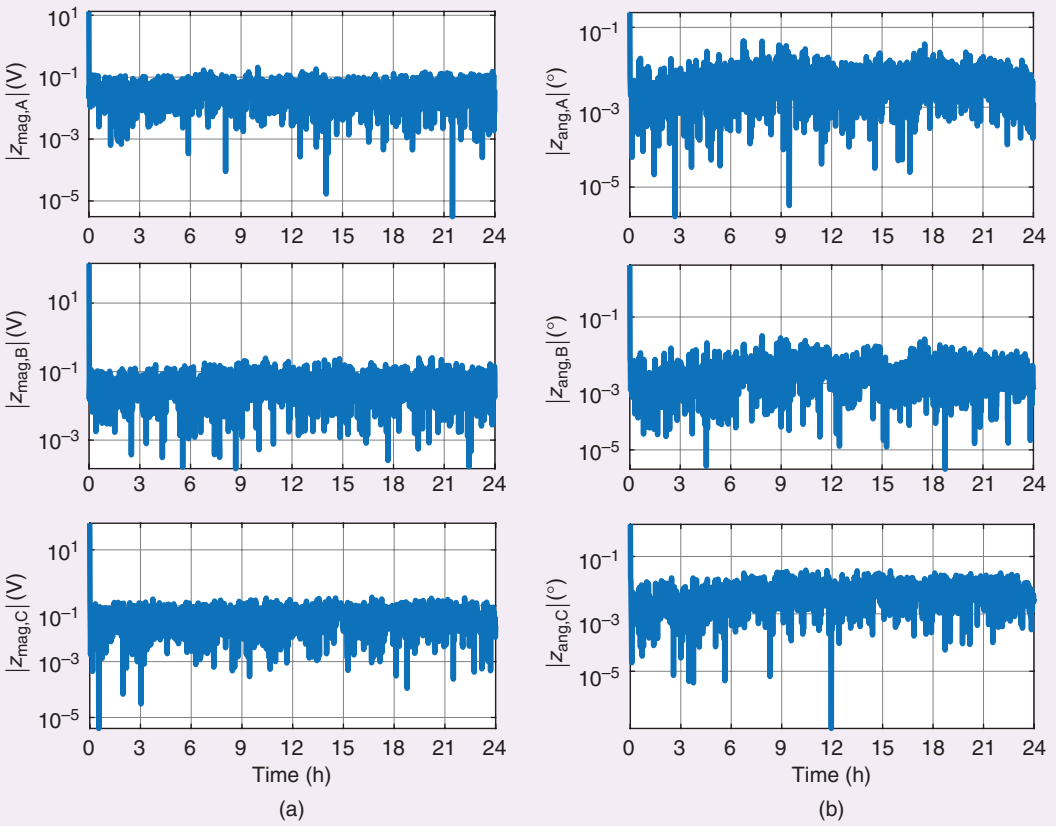

FIGURE 24 Perturbed simulation testing 4: the (a) voltage-magnitude error $|z_{mag}|$ and (b) voltage angle-magnitude error $|z_{ang}|$ for node 671 are shown on a logarithmic scale. Asymptotically, the voltage-magnitude and voltage-angle errors are approximately lower than 0.1 V and 0.01°, respectively.

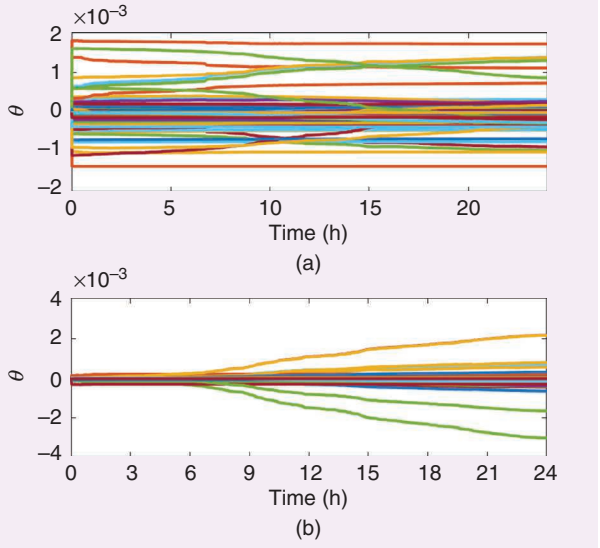

FIGURE 25 Perturbed simulation testing 4: (a) $\theta(k)$ for subcontroller $G_{c1,k}$ and (b) $\theta(k)$ for subcontroller $G_{c2,k}$ are shown.

Based on this approach, the target model used by RCAC was a sparse approximation $\hat{H}_1$ of a single 6×6 impulse-response coefficient H_1. PSTs 1–4 show that $\hat{H}_1$ is robust to changes in the configuration of the actuation and performance nodes. Simulations using the IEEE13NTF model indicate that, with a sparse target model, RCAC provides reliable control with extremely limited modeling information.

To reduce the complexity of the controller for real-time implementation, a fixed-structure extension of RCAC was used, where each SISO entry of each 6×6 MIMO controller was chosen to be either a PI or a second-order IIR controller. RCAC was used in a decentralized architecture, where two subcontrollers were used to follow setpoint commands at physically distinct performance nodes and reject a step-load disturbance at two physically distinct nodes (despite the complete lack of communication between the subcontrollers). For the same scenario, RCAC was shown to be robust to unknown multivariable actuator saturation. Specifically, the two RCAC subcontrollers worked together to achieve a common performance objective despite the limited control authority from each

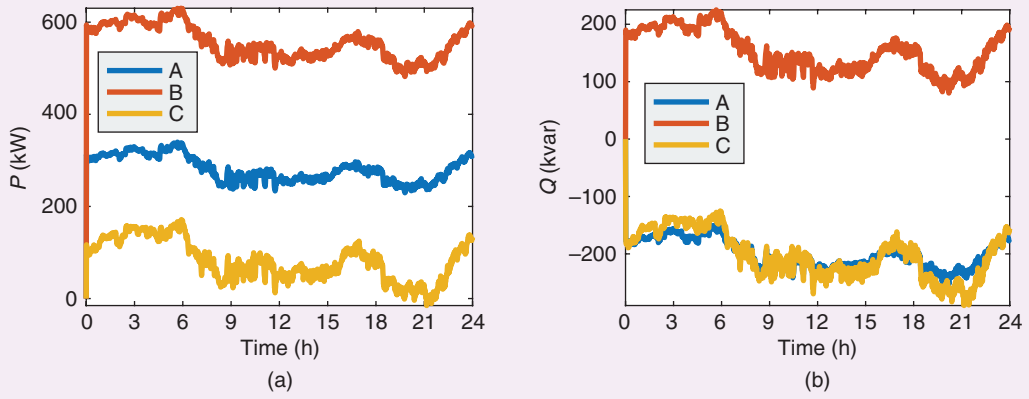

FIGURE 26 Perturbed simulation testing 4: the (a) active and (b) reactive power extracted by subcontroller $G_{c1,k}$ from each phase at node 675 is shown.

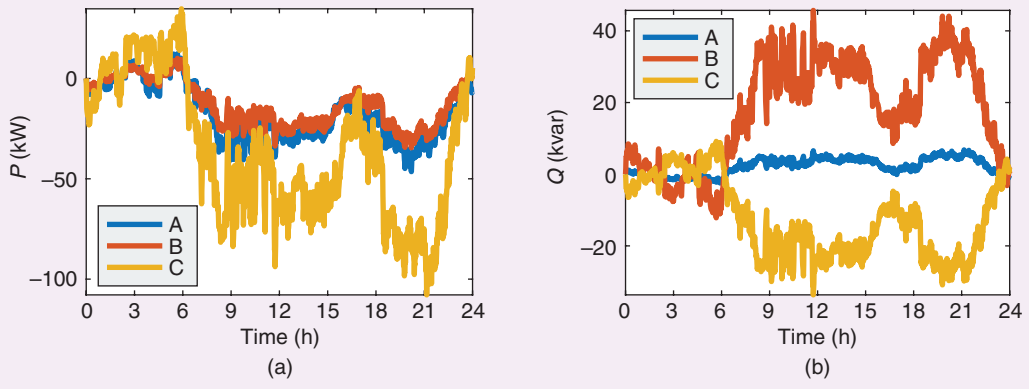

FIGURE 27 Perturbed simulation testing 4: the (a) active and (b) reactive power extracted by subcontroller $G_{c2,k}$ from each phase at node 632 is shown.

controller separately. No adverse interaction between the two controllers was observed. Finally, the ability of two RCAC subcontrollers to follow phasor commands in the presence of 70.61% PV penetration in IEEE13NTF was demonstrated.

Future research will extend IEEE13NTF to include dynamic effects so that it is no longer quasi-static. The goal is to determine the extent of modeling information needed in the presence of unknown dynamics.

ACKNOWLEDGMENTS

The authors are grateful to Alexandra Von Meier for helpful suggestions and discussions. This research was supported by the U.S. Department of Energy under grant DE-EE0008008.

AUTHOR INFORMATION

Syed Aseem Ul Islam (aseemisl@umich.edu) received the B.Sc. degree in aerospace engineering from the Institute of Space Technology, Islamabad, Pakistan, and is currently pursuing the Ph.D. degree in aerospace engineering from the University of Michigan, Ann Arbor. His research interests include data-driven adaptive control for aerospace applications.

Elizabeth L. Ratnam received the B.Eng. (Hons. I) degree in electrical engineering in 2006 and the Ph.D. degree in electrical engineering in 2016 from the University of Newcastle, Australia. She subsequently held postdoctoral research positions with the Center for Energy Research at the University of California, San Diego, and at the University of California, Berkeley, in the California Institute for Energy and Environment. From 2001 to 2012, she held various positions at Ausgrid, a utility that operates one of the largest electricity distribution networks in Australia. She currently holds a Future Engineering Research Leader Fellowship from the Australian National University (ANU), and she joined the Research School of Engineering at ANU as a research fellow and lecturer in 2018. Her research

interests include applications of control theory to power distribution networks.

Ankit Goel received the B.E. degree in mechanical engineering from the Delhi College of Engineering, India, and the Ph.D. degree in aerospace engineering from the University of Michigan, Ann Arbor. His research interests include data-driven estimation and control of high-dimensional complex systems.

Dennis S. Bernstein received the Sc.B. degree in applied mathematics from Brown University, Providence, Rhode Island, and the Ph.D. degree in control engineering from the University of Michigan, Ann Arbor, where he is currently a professor in the Aerospace Engineering Department. His research interests include estimation and control for aerospace applications. He is the author of *Scalar, Vector, and Matrix Mathematics* (Princeton University Press).

REFERENCES

[1] X. Li, D. Hui, and X. Lai, "Battery energy storage station (BESS)-based smoothing control of photovoltaic (PV) and wind power generation fluctuations," *IEEE Trans. Sustain. Energy*, vol. 4, no. 2, pp. 464–473, Apr. 2013.

[2] F. Blaabjerg, R. Teodorescu, M. Liserre, and A. V. Timbus, "Overview of control and grid synchronization for distributed power generation systems," *IEEE Trans. Ind. Elect.*, vol. 53, no. 5, pp. 1398–1409, Oct. 2006.

[3] K. Tanaka et al., "Decentralised control of voltage in distribution systems by distributed generators," *IET Gen. Trans. Distrib.*, vol. 4, no. 11, pp. 1251–1260, 2010.

[4] E. Demirok, D. Sera, R. Teodorescu, P. Rodriguez, and U. Borup, "Evaluation of the voltage support strategies for the low voltage grid connected PV generators," in *Proc. IEEE Energy Conv. Congr. Exposition*, 2010, pp. 710–717.

[5] K. Turitsyn, P. Sulc, S. Backhaus, and M. Chertkov, "Options for control of reactive power by distributed photovoltaic generators," *Proc. IEEE*, vol. 99, no. 6, pp. 1063–1073, 2011.

[6] M. Mills-Price et al., "Solar generation control with time-synchronized phasors," in *Proc. Conf. Protective Relay Engineers*, 2011, pp. 160–167.

[7] M. Savaghebi, A. Jalilian, J. C. Vasquez, and J. M. Guerrero, "Secondary control scheme for voltage unbalance compensation in an islanded droop-controlled microgrid," *IEEE Trans. Smart Grid*, vol. 3, no. 2, pp. 797–807, June 2012.

[8] M. Savaghebi, A. Jalilian, J. C. Vasquez, and J. M. Guerrero, "Autonomous voltage unbalance compensation in an islanded droop-controlled microgrid," *IEEE Trans. Ind. Elect.*, vol. 60, no. 4, pp. 1390–1402, Apr. 2013.

[9] D. E. Olivares et al., "Trends in microgrid control," *IEEE Trans. Smart Grid*, vol. 5, no. 4, pp. 1905–1919, July 2014.

[10] M. A. Abusara, S. M. Sharkh, and J. M. Guerrero, "Improved droop control strategy for grid-connected inverters," *Sustain. Energy Grids Netw.*, vol. 1, pp. 10–19, Mar. 2015.

[11] H. Li, F. Li, Y. Xu, D. T. Rizy, and J. D. Kueck, "Adaptive voltage control with distributed energy resources: Algorithm, theoretical analysis, simulation, and field test verification," *IEEE Trans. Power Syst.*, vol. 25, no. 3, pp. 1638–1647, 2010.

[12] L. B. Perera, G. Ledwich, and A. Ghosh, "Multiple distribution static synchronous compensators for distribution feeder voltage support," *IET Gen. Trans. Distrib.*, vol. 6, no. 4, pp. 285–293, 2012.

[13] A. K. Singh and B. C. Pal, "Decentralized nonlinear control for power systems using normal forms and detailed models," *IEEE Trans. Power Syst.*, vol. 33, no. 2, pp. 1160–1172, Mar. 2018.

[14] D. K. Molzahn et al., "A survey of distributed optimization and control algorithms for electric power systems," *IEEE Trans. Smart Grid*, vol. 8, no. 6, pp. 2941–2962, Nov. 2017.

[15] D. Callaway and I. A. Hiskens, "Achieving controllability of electric loads," *Proc. IEEE*, vol. 99, no. 1, pp. 184–199, Jan. 2011.

[16] W. H. Kersting, "Radial distribution test feeders," in *Proc. IEEE Power and Engineering Society Winter Meeting Conf.*, Jan. 2001, vol. 2, pp. 908–912.

[17] H. Wang and N. N. Schulz, "A revised branch current-based distribution system state estimation algorithm and meter placement impact," *IEEE Trans. Power Syst.*, vol. 19, no. 1, pp. 207–213, Feb. 2004.

[18] F. Jurado, "Modeling SOFC plants on the distribution system using identification algorithms," *J. Power Sources*, vol. 129, no. 2, pp. 205–215, 2004.

[19] S. Moghaddas-Tafreshi and E. Mashhour, "Distributed generation modeling for power flow studies and a three-phase unbalanced power flow solution for radial distribution systems considering distributed generation," *Elec. Power Syst. Res.*, vol. 79, no. 4, pp. 680–686, 2009.

[20] M. Abdel-Akher and K. M. Nor, "Fault analysis of multiphase distribution systems using symmetrical components," *IEEE Trans. Power Del.*, vol. 25, no. 4, pp. 2931–2939, Oct. 2010.

[21] S. Paudyal, C. A. Canizares, and K. Bhattacharya, "Optimal operation of distribution feeders in smart grids," *IEEE Trans. Ind. Electron.*, vol. 58, no. 10, pp. 4495–4503, Oct. 2011.

[22] S. Gautam and S. M. Brahma, "Detection of high impedance fault in power distribution systems using mathematical morphology," *IEEE Trans. Power Syst.*, vol. 28, no. 2, pp. 1226–1234, May 2013.

[23] I. Dzafic, M. Gilles, R. A. Jabr, B. C. Pal, and S. Henselmeyer, "Real time estimation of loads in radial and unsymmetrical three-phase distribution networks," *IEEE Trans. Power Syst.*, vol. 28, no. 4, pp. 4839–4848, Nov. 2013.

[24] H. Yazdanpanahi, Y. W. Li, and W. Xu, "A new control strategy to mitigate the impact of inverter-based DGs on protection system," *IEEE Trans. Smart Grid*, vol. 3, no. 3, pp. 1427–1436, Sept. 2012.

[25] O. Ardakanian, S. Keshav, and C. Rosenberg, "Real-time distributed control for smart electric vehicle chargers: From a static to a dynamic study," *IEEE Trans. Smart Grid*, vol. 5, no. 5, pp. 2295–2305, Sept. 2014.

[26] I. Sharma, K. Bhattacharya, and C. Canizares, "Smart distribution system operations with price-responsive and controllable loads," *IEEE Trans. Smart Grid*, vol. 6, no. 2, pp. 795–807, Mar. 2015.

[27] T. Morstyn, B. Hredzak, and V. G. Agelidis, "Distributed cooperative control of microgrid storage," *IEEE Trans. Power Syst.*, vol. 30, no. 5, pp. 2780–2789, Sept. 2015.

[28] B. Millar, D. Jiang, and M. E. Haque, "Constrained coordinated distributed control of smart grid with asynchronous information exchange," *J. Mod. Power Syst. Clean Energy*, vol. 3, no. 4, pp. 512–525, Dec. 2015.

[29] J. R. Castro, M. Saad, S. Lefebvre, D. Asber, and L. Lenoir, "Optimal voltage control in distribution network in the presence of DGs," *Int. J. Elec. Power Energy Syst.*, vol. 78, pp. 239–247, June 2016.

[30] A. Ghavami, K. Kar, and A. Gupta, "Decentralized charging of plug-in electric vehicles with distribution feeder overload control," *IEEE Trans. Autom. Control*, vol. 61, no. 11, pp. 3527–3532, Nov. 2016.

[31] ePHASORSIM. Accessed on: Oct. 2018. [Online]. Available: https://www.opal-rt.com/systems-ephasorsim/

[32] Y. Rahman, A. Xie, and D. S. Bernstein, "Retrospective cost adaptive control: Pole placement, frequency response, and connections with LQG control," *IEEE Control Syst. Mag.*, vol. 37, pp. 28–69, Oct. 2017.

[33] J. B. Hoagg and D. S. Bernstein, "Retrospective cost model reference adaptive control for nonminimum-phase systems," *J. Guid. Control Dyn.*, vol. 35, no. 6, pp. 1767–1786, 2012.

[34] S. A. Ul Islam and D. S. Bernstein, "Output-feedback adaptive control of discrete-time systems with unknown, unmatched, inaccessible nonlinearities," in *Proc. American Control Conf.*, Milwaukee, WI, June 2018, pp. 1695–1700.

[35] J. Yan and D. S. Bernstein, "Minimal modeling retrospective cost adaptive control of uncertain hammerstein systems using auxiliary nonlinearities," *Int. J. Control*, vol. 87, pp. 483–505, 2014. doi: 10.1080/00207179.2013.842264.

[36] Pecan Street. Accessed on: Oct. 2018. [Online]. Available: http://www.pecanstreet.org/